

JGR Solid Earth

RESEARCH ARTICLE

10.1029/2021JB021966

Special Section:

Ophiolites and Oceanic Lithosphere, with a focus on the Samail ophiolite in Oman

Key Points:

- The H₂O–CO₂ contents of volcanic glasses in the ophiolites are used to estimate ocean depths during lava extrusion on the seafloor
- Ocean depth during volcanism is constrained to between 3.2 and 4.0 km for the Samail ophiolite and 3.6 and 4.9 km for the Troodos ophiolite
- High seafloor fluid pressures may have allowed convecting hydrothermal fluids to reach temperatures above 450°

Supporting Information:

Supporting Information may be found in the online version of this article.

Correspondence to:

T. M. Belgrano,
t.belgrano@soton.ac.uk

Citation:

Belgrano, T. M., Tollan, P. M., Marxer, F., & Diamond, L. W. (2021). Paleobathymetry of submarine lavas in the Samail and Troodos ophiolites: Insights from volatiles in glasses and implications for hydrothermal systems. *Journal of Geophysical Research: Solid Earth*, 126, e2021JB021966. <https://doi.org/10.1029/2021JB021966>

Received 26 FEB 2021

Accepted 29 JUN 2021

© 2021. The Authors.

This is an open access article under the terms of the [Creative Commons Attribution](https://creativecommons.org/licenses/by/4.0/) License, which permits use, distribution and reproduction in any medium, provided the original work is properly cited.

Paleobathymetry of Submarine Lavas in the Samail and Troodos Ophiolites: Insights From Volatiles in Glasses and Implications for Hydrothermal Systems

Thomas M. Belgrano^{1,2} , Peter M. Tollan^{2,3}, Felix Marxer^{4,3} , and Larry W. Diamond² 

¹School of Ocean and Earth Science, National Oceanography Centre Southampton, University of Southampton, Southampton, UK, ²Institute of Geological Sciences, University of Bern, Bern, Switzerland, ³Institute of Geochemistry and Petrology, ETH Zurich, Zurich, Switzerland, ⁴Institute of Mineralogy, Leibniz University Hannover, Hannover, Germany

Abstract Hydrostatic pressure exerted by the ocean water column fundamentally influences magmatic and hydrothermal processes in submarine volcanic settings and is therefore an important parameter to know when investigating such processes. Currently, there are few reliable methods for reconstructing past ocean depths for ancient volcanic terranes. Here, we develop and test an empirically calibrated statistical approach for determining paleodepths of eruption from the concentrations of H₂O and CO₂ dissolved in volcanic glasses, utilizing the well-defined pressure-dependent solubility of these volatiles in silicate melts. By comparing newly determined and published glass compositions from the Samail and Troodos ophiolites with sedimentary and fluid inclusion evidence, we propose that the Samail lavas erupted at ocean depths of ~3.4 km, and the Troodos lavas at ~4.1 km. These depths are 1–2 km deeper than those assumed in most previous studies of hydrothermal activity in the two ophiolites. These high depths imply high hydrostatic pressures within the underlying oceanic crust. Such pressures may have allowed convecting hydrothermal fluids to attain significantly higher temperatures (e.g., >450°C) than in typical modern ocean ridge hydrothermal systems during metal leaching in the crust and metal precipitation in seafloor sulfide deposits.

Plain Language Summary The pressure of seawater exerts a fundamental influence on volcanism and related processes in Earth's oceanic crust. This article presents an improved method for estimating the depth of seawater above ancient oceanic volcanic rocks as they were forming. Determining these depths allows us to better define the pressure under which this ancient crust formed and hence more accurately model it and compare it to modern examples.

1. Introduction

Studies of the Samail and Troodos ophiolites have greatly influenced our interpretation of the formation, hydrothermal alteration, and ore mineralization of oceanic crust (e.g., Gillis & Banerjee, 2000; Hannington et al., 1998; Pearce et al., 1984). Pressure fundamentally influences these processes and is a necessary parameter to know for many of the models and tools we use to describe and investigate them (e.g., Jupp & Schultz, 2004; Monecke et al., 2014). Despite this necessity, few methods are available for estimating paleodepths of seawater in ancient, open ocean volcanic terranes (Monecke et al., 2014). This paper aims to present an improved paleobathymetric approach for ancient seafloor lava eruptions and to apply it to the archetypal Samail (Oman–UAE) and Troodos (Cyprus) ophiolites.

For submarine volcanic terranes that accumulated below storm wave base, the three most promising lines of paleobathymetric evidence are the sedimentary record (e.g., pelagic carbonates indicating depths shallower than the carbonate compensation depth (CCD); Robertson, 2004), fluid inclusion evidence (e.g., in inclusions trapped in minerals formed at the seafloor; Spooner, 1980), and the concentrations of volatiles dissolved in volcanic glasses, which are partly dependent on pressure during quenching (Roberge et al., 2005). In the following, we determine the dissolved H₂O concentrations and maximum permissible CO₂ concentrations of volcanic glasses from the Samail ophiolite, and interpret these in terms of paleodepths of eruption together with a similar, recently published data set from the Troodos ophiolite (Woelki et al., 2020). We then compare these predictions to sedimentary and fluid inclusion evidence from both ophiolites, finding

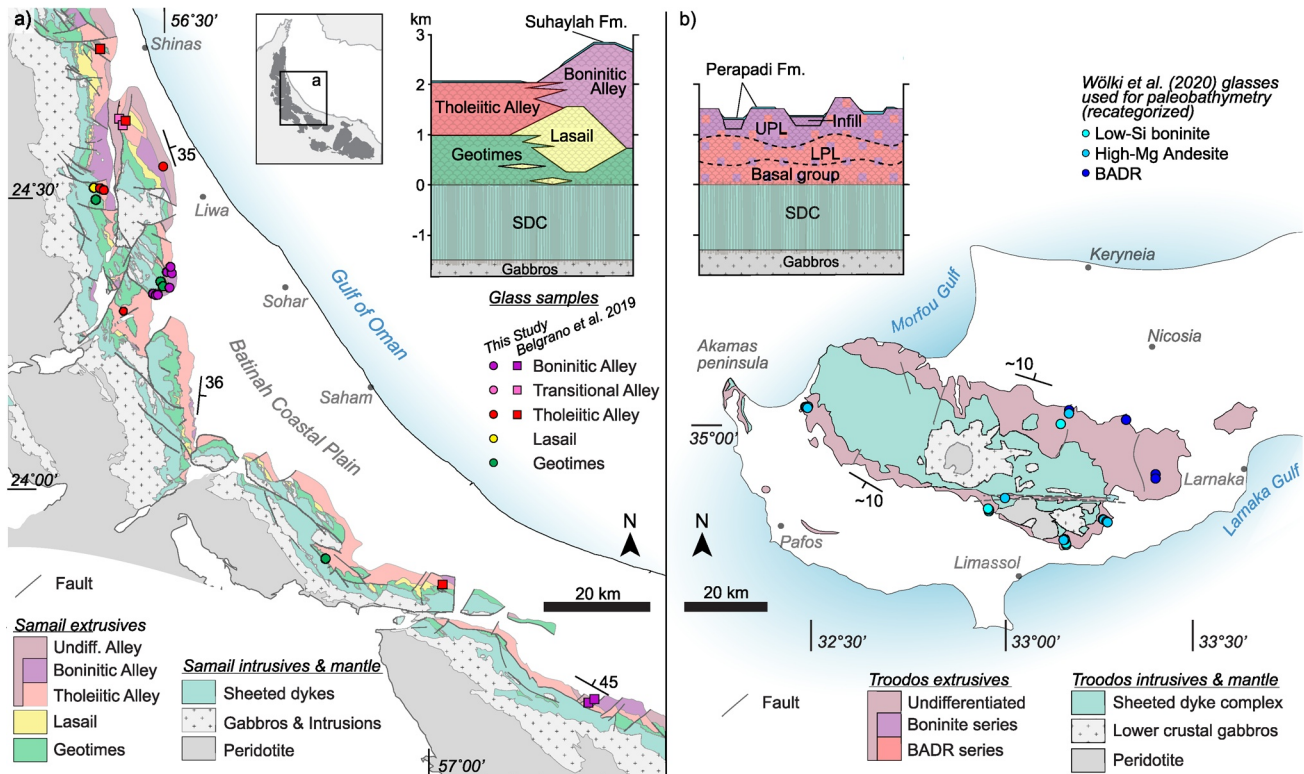


Figure 1. Maps, glass locations, and upper crustal pseudo-stratigraphies of the Samail and Troodos ophiolites. (a) Bedrock geological map and upper crustal stratigraphy of the northeastern (Batinah Coast) region of the Samail ophiolite, simplified after Belgrano et al. (2019). Inset shows entire ophiolite (dark grey) on Arabian Peninsula. (b) Geological map of the Troodos ophiolite simplified from Cyprus Geological Survey Department (1995) and Osozawa et al. (2012). Glass sample locations used for paleobathymetry from Wölki et al. (2020), recategorized for this study. BADR = Basalt-Andesite-Dacite-Rhyolite. Upper crustal stratigraphy adapted from Cyprus Geological Survey Department (1995) and Gass et al. (1994); see Section 1.1.2 for details.

that the volatiles-in-glass and sedimentary records agree. Much of the fluid inclusion evidence is compatible with these interpretations, but there are also conflicting cases. The potential reasons for these discrepancies are discussed, together with the implications of these results for interpreting the tectonic setting of ophiolites as well as the fossil hydrothermal systems and the known gold enrichment in the volcanogenic massive sulfide (VMS) deposits they host.

1.1. Ophiolite Magmatic Evolution and Volcanostratigraphy

1.1.1. Samail Ophiolite

Magmatism along a seafloor spreading axis formed much of the lower crust as well as the sheeted-dike complex and comagmatic “Geotimes” basal lava unit (Pearce et al., 1981; Umino et al., 1990). These dikes and lavas are similar in trace element composition to mid-ocean ridge basalts (MORB), but show a broader range of SiO₂ compositions and are subtly contaminated by a hydrous subduction component (Belgrano et al., 2019; MacLeod et al., 2013; Pearce et al., 1981). Locally, axial magmatism was more substantially contaminated by subduction fluids, resulting in the eruption of high Th/Nb “Axial Lasail” basalts depleted in incompatible trace elements (Belgrano & Diamond, 2019).

Some areas of the axial crust (Figure 1a) were then immediately overlain by off-axial “Lasail” unit basalts (Alabaster et al., 1982; Belgrano et al., 2019). Post-axial lavas buried this entire sequence, and can be split into lower “Tholeiitic Alley” and upper “Boninitic Alley” units based on stratigraphy and composition (Belgrano et al., 2019; Gilgen et al., 2014; Ishikawa et al., 2002; Kusano et al., 2014). Where preserved, the top of the volcanic sequence is conformably capped by umbers and pelagic sediments of the Suhaylah formation (Robertson & Fleet, 1986). The plutonic equivalents of this volcanic sequence crystallized between 96.5–

95.0 Ma (Rioux et al., 2013, 2021), and this occurred entirely in a supra-subduction zone, possibly proto-arc, tectonic setting (Belgrano & Diamond, 2019; MacLeod et al., 2013; Rioux et al., 2016). The final volcanic phase, the “*Salahi*” (“V3”) lava unit, was geographically limited and occurred several million years after the regional-scale Boninitic Alley volcanism (Hara & Kurihara, 2017; Umino, 2012), so is not mentioned further here. The map distribution, volcanostratigraphy and the typical unit thicknesses for the northern and central Samail ophiolite are summarized in Figure 1a.

1.1.2. Troodos Ophiolite

The Troodos volcanic sequence was initially divided into mappable units of the “*Basal Group*”, comprising a transition zone between the sheeted dike complex and the extrusives, the “*Lower Pillow Lavas*”, and the “*Upper Pillow Lavas*” (Cyprus Geological Survey Department, 1995). Other authors also differentiated boninitic “*Infill lavas*”, which fill structural depressions at the top of the volcanic sequence (Cameron, 1985; Gass et al., 1994). The Troodos volcanostratigraphy records a general evolution from basalt–andesite–dacite–rhyolite (BADR) series tholeiites to highly depleted boninites (Pearce & Robinson, 2010; Regelous et al., 2014). This geochemical evolution is not perfectly continuous, however, and does not strictly correspond with the originally mapped units: Boninites exist within the mostly BADR series Basal & Lower Pillow Lavas, and high-Ti tholeiites can be found within the mostly boninite series Upper Pillow lavas (Portnyagin et al., 1997; Regelous et al., 2014; Woelki et al., 2018). This general volcanic progression is schematically illustrated in the upper-crustal stratigraphy in Figure 1b along with a map of the undifferentiated volcanic rocks. Recent dating suggests that the Troodos magmatism was underway by 94.3 ± 0.5 Ma (Morag et al., 2020), and that this probably occurred in either a proto-arc or fore-arc, supra-subduction zone tectonic setting (e.g., Pearce & Robinson, 2010; Robinson et al., 1983; Woelki et al., 2018).

2. Samples, Methods & Data

2.1. Samail Volcanic Glass Samples

Pristine volcanic glasses are exceedingly rare in the Samail lavas (Kusano et al., 2017). Our field sampling throughout the Samail ophiolite (Belgrano et al., 2019) confirmed that glass is rare, but is most likely to be preserved in areas with sub-greenschist facies hydrothermal alteration, hence mostly within the upper Alley group volcanic units (Figure 2). All the glasses we collected from the axial Geotimes lavas were subtly affected by secondary hydration, though one pristine glass was recovered from Axial Lasail lavas intercalated within the uppermost axial Geotimes sequence, near similar intercalations along Wadi Fizh (Belgrano & Diamond, 2019). Where present, glass is most commonly preserved in the crusts of pillow lavas or in hyaloclastite breccias as black glassy spheroids and chips within a brown palagonitized matrix (Figures 2a–2c). None of the pristine glass samples derive from massive flows.

The freshest chips of glass were mounted in epoxy, then polished and used for electron microprobe analysis (EMPA). Following EMPA the mounts were cut into 80–250 μm thick wafers and polished on their opposite side for Fourier transform infrared (FTIR) analysis in transmission mode. Of 40 glass samples collected from the Samail lava units, only 23 contained areas free of phenocrysts, suitable for FTIR analysis (Figure 3). Of these, FTIR spectra revealed that only 17 samples from the Lasail and Alley group units were pristine and therefore useful for paleobathymetry (supporting information, Figures S1 and S2).

2.2. Troodos Volcanic Glass Data

The Troodos volcanic glass volatile data used in this study are taken from Woelki et al. (2020), who also measured major elements by EMPA and $\text{H}_2\text{O}-\text{CO}_2$ by FTIR. Of their 43 reported compositions, 38 are pristine based on their ratios of molecular H_2O ($\text{H}_2\text{O}_{\text{mol}}$) to total H_2O , and only these 38 were used for paleobathymetry (supporting information, Figure S2). Other studies on H_2O in Troodos lavas and glasses were not used because they (a) were not able to verify the pristine nature of the glasses, or (b) did not report CO_2 contents or limits of detection (LOD), or (c) reported only whole-rock values, or (d) determined CO_2

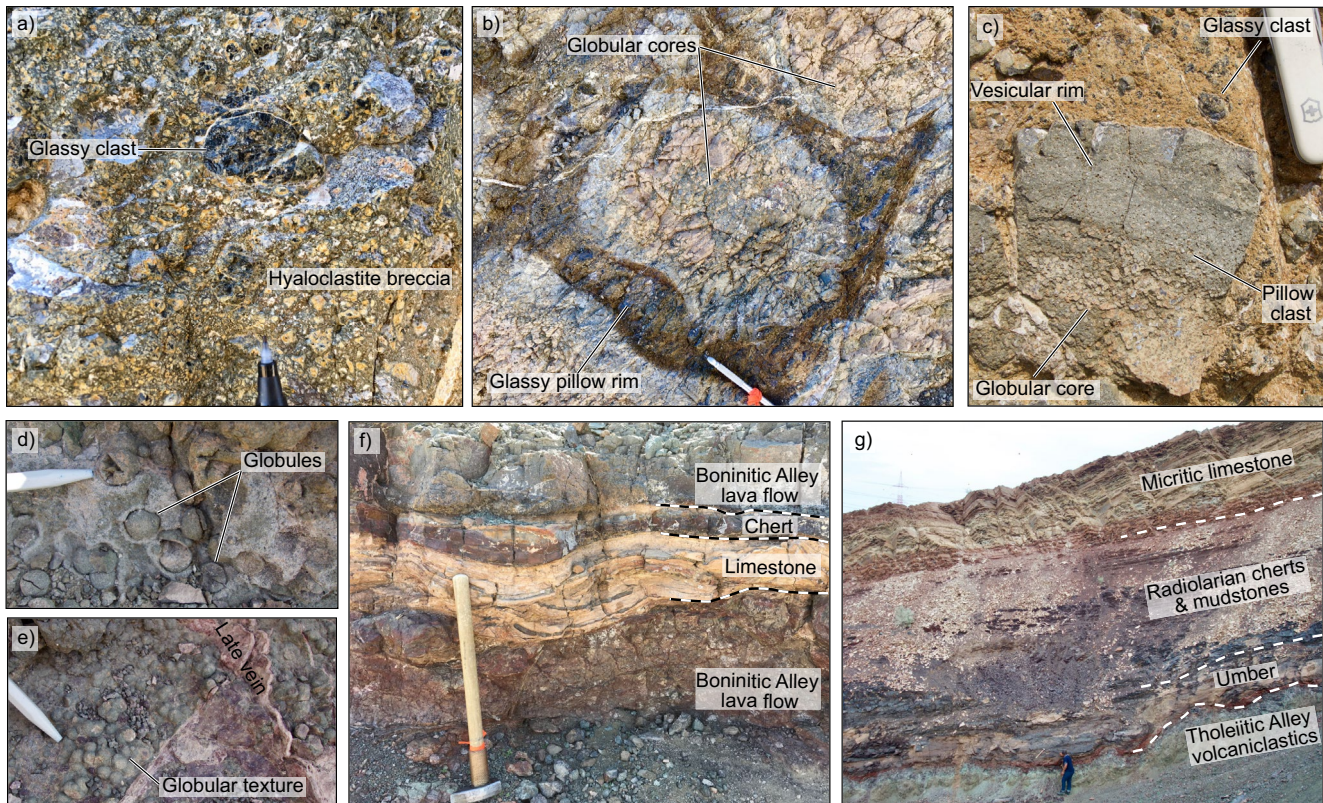


Figure 2. Field photos from the Samail ophiolite. (a) Typical glassy clast preserved in a hyaloclastite breccia exposed in a roadcut (Sample TB5-40B; 56.4256°E, 24.6223°N). (b) Well-preserved glassy rim around a globular textured Tholeiitic Alley pillow lava (Sample TB5-36B; 56.4980°E, 24.5466°N). (c) Pillow lava clast with vesicular rim and globular core and other glassy clasts in a palagonitised hyaloclastite matrix (24.7624°E, 56.3741°N). (d and e) Globular textures in Boninitic Alley lavas (24.118°E, 56.561°N). (f) Syn-volcanic limestone and chert interbedded with Boninitic Alley lava flows near Wadi Jizi (~24.332°E 56.487°N). (g) Suhaylah Formation (top-ophiolite) showing the most common progression from umber to radiolarian cherts to calcareous limestones (type locality, 24.2642°E, 56.3556°N).

contents by fusion mass spectrometry, which is known to systematically overestimate CO₂ contents in glasses (Newman et al., 2000).

2.3. Electron Microprobe Analyses

Major element glass compositions for a subset of the Samail glasses were reported in Belgrano et al. (2019). The remainder of the Samail glasses were measured by EMPA at either the University of Bern or ETH Zürich. Measurements at the University of Bern were performed identically to Belgrano et al. (2019), using a Jeol™ JXA-8200 with a beam voltage of 15 kV, a beam current of 10 nA, and a beam diameter of 10 μm (0.13 nA/μm²). The standards used were natural wollastonite (Si, Ca), albite (Na), orthoclase (K) and chrome spinel (Cr), and synthetic olivine (Mg, Fe), anorthite (Al), tephroite (Mn), and ilmenite (Ti). EMPA measurements at ETH Zürich were carried out using a JEOL™ JXA-8230 with a beam voltage of 15 kV, a beam current of 5 nA, and a beam diameter of 20 μm (0.016 nA/μm²). The standards used were natural Albite (Si, Na), Anorthite (Ca, Al), microcline (K) and chrome spinel (Cr), and synthetic fayalite (Fe), forsterite (Mg), rutile (Ti), and pyrolusite (Mn). Current densities well below 0.5 nA/μm² were used to avoid Na loss during measurement (Morgan & London, 2005). Assuming a back-arc basalt like Fe³⁺/Fe_{total} ratio of 0.2 (Brounce et al., 2014), measured oxide plus H₂O totals for the glasses sum to 97.4–100.6 wt%. The shortfall of ≤ 2.6 wt% can be explained by the sum of several unmeasured minor elements (P, S, Cl, V), which make up ~0.5–2 wt% of glasses from similar settings (Jenner et al., 2015; Woelki et al., 2020), together with a ~1 wt% total shortfall related to matrix differences between the crystal standards and the glasses (Hughes et al., 2019).

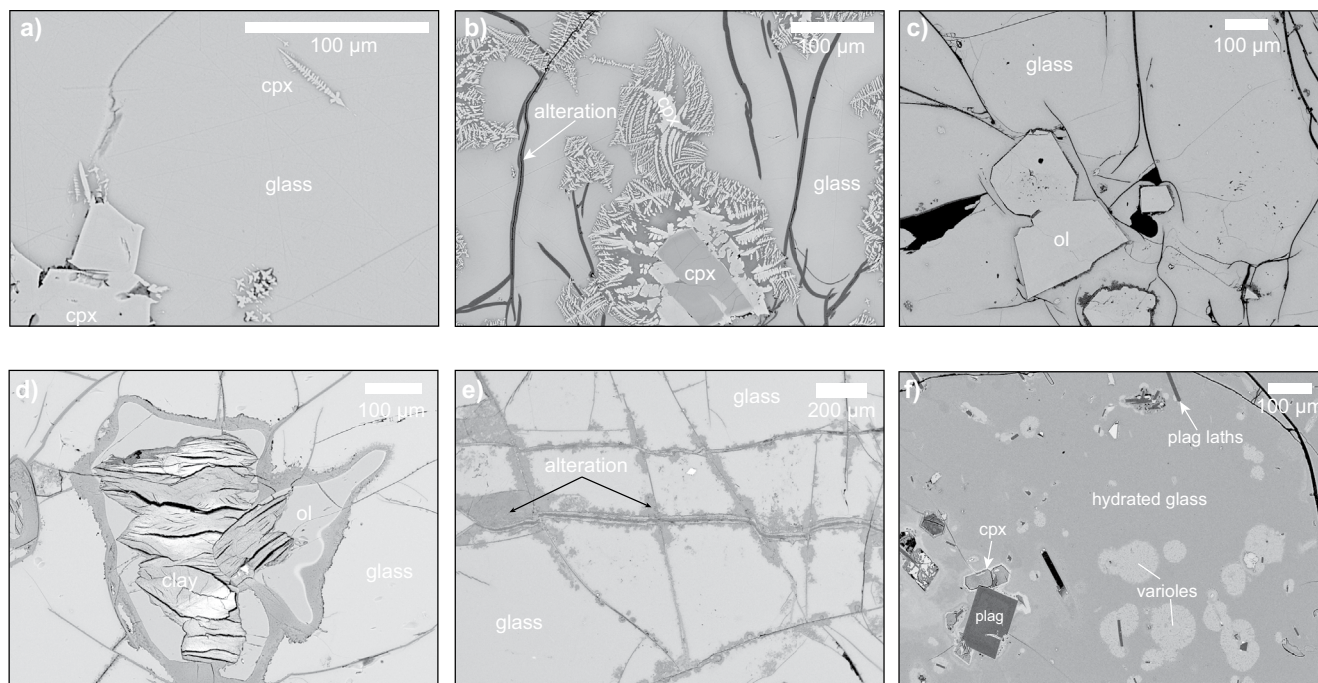


Figure 3. Back-scattered electron images of Samail glasses. (a) Entirely pristine glass from the Tholeiitic Alley unit (TB4-16B) with a clinopyroxene (cpx) phenocryst and skeletal microlites. (b) Mostly pristine glass and skeletal cpx from the Boninitic Alley unit (TB4-19E). Incipient alteration along cracks was avoided during analysis. (c) Axial Lasail unit glass (TB6-03C) with fresh olivine (ol) phenocrysts and incipient alteration along cracks. (d) Olivine altered mostly to clay in a matrix of mostly pristine glass from the Tholeiitic Alley unit (TB4-12A). (e) Tholeiitic Alley glass (TB4-08D) with alteration along cracks separating domains of fresh glass several hundred μm wide. (f) Geotimes glass (TB6-03A) with alteration around phenocrysts and a subtly textured hydrated matrix. This kind of glass was not used for paleobathymetry.

2.4. Fourier Transform Infrared Spectroscopy

Dissolved H_2O and CO_2 concentrations in volcanic glasses were determined by transmission FTIR spectrometry at the University of Bern, using a Bruker™ Tensor 27 spectrometer with a globar infrared source and KBr beamsplitter connected to a Bruker™ Hyperion 3000 microscope. A liquid nitrogen-cooled mercury-cadmium-telluride detector collected spectra from an average of 64 scans, acquired from 400 to $6,000\text{ cm}^{-1}$ at 8 cm^{-1} resolution over square analysis areas with side lengths of 20 – $100\text{ }\mu\text{m}$. The sample chamber was purged continuously with dry air and background measurements were taken regularly and subtracted from the measured spectra. Concentrations of dissolved species in the glasses were calculated using the Beer-Lambert equation (see von Aulock et al., (2014) for a review of its parameters).

2.4.1. Dissolved H_2O

Total dissolved H_2O was determined by summing the concentrations of $\text{H}_2\text{O}_{\text{mol}}$ and OH^- , calculated from non-integrated absorbance of bands centered at $1,630\text{ cm}^{-1}$ and $4,500\text{ cm}^{-1}$ respectively. Use of the total H_2O band at $3,500\text{ cm}^{-1}$ was not possible because of excessive absorption at this wavenumber for the prepared wafer thicknesses. For glasses affected by secondary hydration (see below), excess absorption also occurred at $1,630\text{ cm}^{-1}$, so the $\sim 5,430\text{ cm}^{-1}$ $\text{H}_2\text{O}_{\text{mol}}$ band was used instead for the total H_2O calculation. In order to calculate the non-integrated absorbances, a flexicurve baseline was manually drawn under each band using the polynomial baseline correction tool of the OPUS (Bruker™) software (supporting information, Figure S1).

Absorption coefficients for the $\text{H}_2\text{O}_{\text{mol}}$ and OH^- bands were calculated for each glass using the Mandeville et al. (2002) regressions of absorption coefficient to “tau”, the molar ratio of tetrahedral to total cations. Wafer thickness was measured using a Mitutoyo™ digital depth gauge. The density of each glass was calculated from the summation of major element oxide partial molar volumes after Lange and Carmichael (1987) and Ochs and Lange (1999), with H_2O defined by one iteration of the FTIR results.

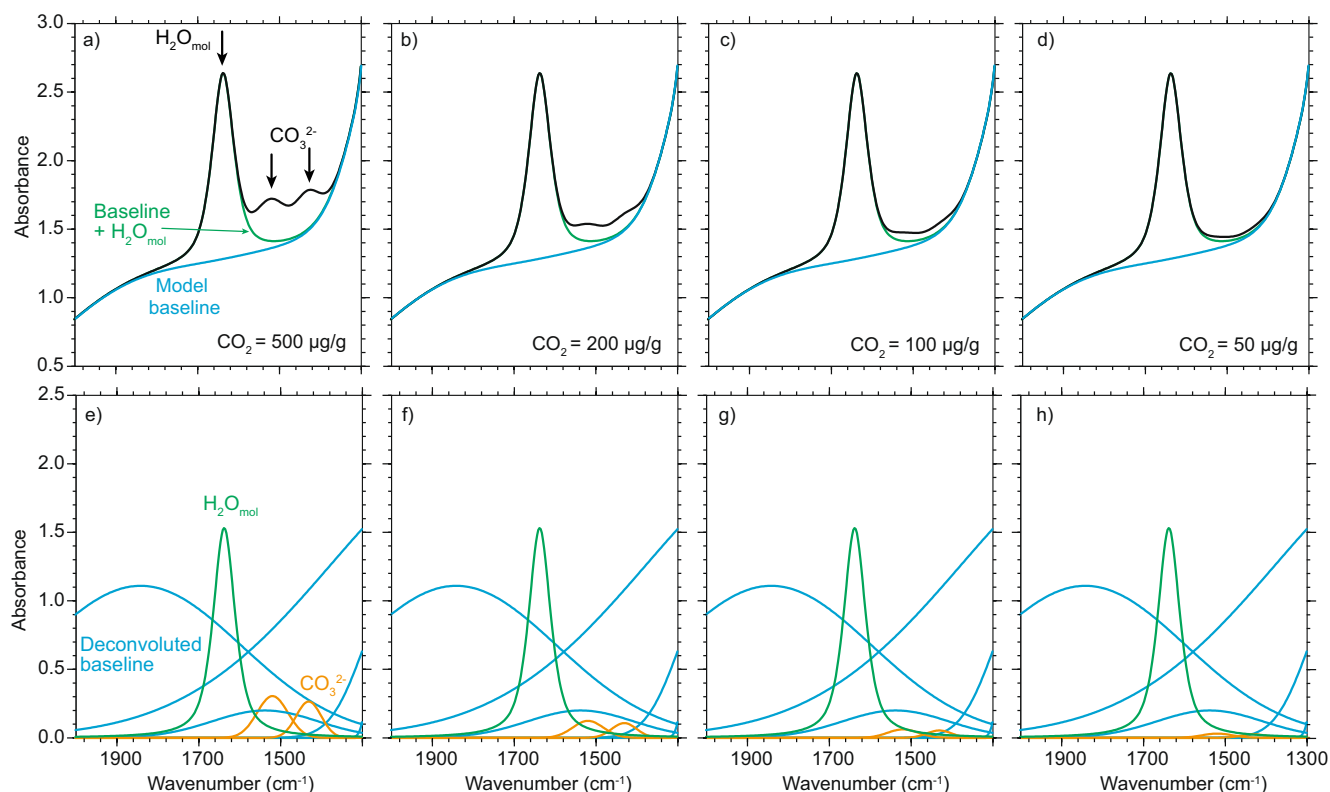


Figure 4. Examples of a deconvolution exercise to calculate CO_2 concentrations and to estimate the lower limit of detection for CO_2 . (a–d) Show a modelled Samail glass spectrum (see examples in supporting information, Figure S3) with varying amounts of CO_2 added in the form of CO_3^{2-} (bands at 1,520 and 1,430 cm^{-1}). The blue line shows the deconvoluted baseline. The green line shows this baseline plus typical $\text{H}_2\text{O}_{\text{mol}}$ absorbance (0 $\mu\text{g/g}$ CO_2). The black line shows the effect of adding 50–500 $\mu\text{g/g}$ CO_2 to the total absorbance spectra. (e–h) show the individual deconvoluted bands that comprise the baseline (blue), $\text{H}_2\text{O}_{\text{mol}}$ (green) and CO_3^{2-} (orange). The sum of all these bands is equal to the black line in a) to d). See Section 2.4.2 and Supporting Information, Figures S3 and S4 for further detail and examples.

Intra-sample variability and measurement precision are summarized by 1σ errors between 1%–6% relative standard deviation (RSD) for the pristine glasses. Uncertainty propagated through the Beer–Lambert calculation for total H_2O is 15%–20%, in agreement with Dixon et al. (1995).

To verify the pristine state of the Samail glasses and the accuracy of our data, we compared the measured concentrations of $\text{H}_2\text{O}_{\text{mol}}$, OH^- and H_2O to experimentally defined model relationships for these species in basaltic glasses (supporting information, Figure S2; Dixon et al., 1995). Over the 1.5–2.6 wt% H_2O range, our data fit the models well and have RSD <6%, so these are considered to be pristine glasses. Six glasses plot at much higher H_2O (5–8 wt%), have variably higher $\text{H}_2\text{O}_{\text{mol}}/\text{OH}^-$ ratios than the pristine model, and have much higher within-sample variability. Together these factors are strongly suggestive of secondary hydration, and these glasses were accordingly not used for paleobathymetry. All glasses from the Geotimes unit were affected by this secondary hydration.

2.4.2. Dissolved CO_2

Quantification of dissolved CO_2 in hydrous volcanic glasses by FTIR is challenging because the 1,520 and 1,430 cm^{-1} CO_3^{2-} bands coincide both with baseline curvature and an overlapping peak tail from $\text{H}_2\text{O}_{\text{mol}}$ at 1,630 cm^{-1} (Figure 4). These problems are exacerbated at low CO_2 concentrations approaching the LOD (<100 $\mu\text{g/g}$), yet studies reporting such concentrations of CO_2 in basaltic glasses typically provide few details on how the CO_3^{2-} bands were quantified. Some studies refer to the subtraction of a devolatilized reference glass from the sample spectrum, or spectral deconvolution using an unpublished spreadsheet (e.g., Woelki et al., 2020), likely based on Newman et al. (2000). Below we show that subtraction of a devolatilized baseline may be insufficient for quantifying such low CO_2 concentrations, and that spectral deconvolution is also limited to some extent by baseline uncertainty.

Strong and unambiguous absorption bands related to CO_3^{2-} were absent in all of the Samail glasses, irrespective of the wafer thicknesses (80–250 μm). Given the importance of constraining CO_2 concentrations for bathymetry, we conducted a modelling exercise using a set of experimental basaltic glasses containing various concentrations of H_2O and CO_2 , including a nominally volatile-free glass, in order to estimate the LOD for CO_2 . The experimental glasses have a target composition of basalt sample RDC156 in Hürlimann et al. (2016), and volatile saturation was targeted (see Ulmer et al. (2018) and Supplement for more details). All calculations used the non-integrated, thickness-normalized absorbance obtained directly from the deconvolution models and a molar absorption coefficient for basalt of $375 \text{ l mol}^{-1} \text{ cm}^{-1}$ (Fine & Stolper, 1986).

We initially attempted to subtract the spectrum of the devolatilized experimental basalt from the spectra of the volatile-bearing experimental glasses. Despite these glasses having exactly the same composition, we found that the baseline curvature was sufficiently different that the CO_3^{2-} absorption would be grossly obscured. If applied to low (<100 $\mu\text{g/g}$) CO_2 glasses, any subtle absorption related to CO_3^{2-} would not be possible to resolve.

Instead, we produced a spectral deconvolution model using both the devolatilized and variably volatile-bearing experimental glasses, which was then applied to the Samail glasses in order to estimate CO_2 concentrations and LOD. Initially, we deconvoluted the volatile-free glass to generate a flexible baseline model that could be adapted to other glasses (Supporting Information, Figure S3). This was performed using a linear least squares regression analysis, solving for six Gaussian bands with variable halfwidths and band centers. Taking this baseline model, we applied it to the H_2O and CO_2 -bearing experimental glasses with their subtly different baselines, allowing the band halfwidths and heights to vary until the residual term was minimized. We then introduced three additional bands to account for absorption related to $\text{H}_2\text{O}_{\text{mol}}$ and CO_3^{2-} . This allowed us to create a generalized model of an H_2O – CO_2 bearing glass which could be applied to the Samail glasses (Supporting Information, Figure S4). To back-check the accuracy of this model, we deconvoluted the volatile-free glass again, this time including the bands for $\text{H}_2\text{O}_{\text{mol}}$ and CO_3^{2-} , with the CO_3^{2-} 1,430/1,520 cm^{-1} band ratio fixed at 0.87 (the average from CO_2 -bearing glass models). This model generated absorption equivalent to 0.0 wt% $\text{H}_2\text{O}_{\text{mol}}$ and 7 $\mu\text{g/g}$ CO_2 , indicating that our model does not add CO_3^{2-} bands in any significant amount to compensate for intrinsic baseline curvature.

We applied this deconvolution routine to all the pristine Samail glass spectra. Modelled CO_2 concentrations were mostly below 50 $\mu\text{g/g}$. What these low CO_2 concentrations represent is a critical question: detectable CO_2 or artefacts from the model to compensate for the overlapping $\text{H}_2\text{O}_{\text{mol}}$ band? To understand this, we took the baseline + $\text{H}_2\text{O}_{\text{mol}}$ model of a typical Samail glass and added varying amounts of CO_3^{2-} absorbance, reflecting CO_2 concentrations from 500–50 $\mu\text{g/g}$ (Figure 4). Qualitatively, the impact of the CO_3^{2-} bands is still evident at 100 $\mu\text{g/g}$ CO_2 . At 50 $\mu\text{g/g}$ CO_2 , the spectrum is impacted but the individual bands are unclear and the deconvoluted CO_3^{2-} bands have similar absorbance to the overlapping $\text{H}_2\text{O}_{\text{mol}}$ tail (Figure 4h). Combined with the deconvolution results of the Samail glasses, we thus estimate a LOD of $\sim 50 \mu\text{g/g}$. Variation modelled below 50 $\mu\text{g/g}$ may reflect inaccuracies in the baseline or $\text{H}_2\text{O}_{\text{mol}}$ deconvolution rather than actual variations in CO_2 , so are not reported. We emphasize that this is a strictly qualitative estimate of LOD with a degree of ambiguity. Rigorously determining a LOD would require a suite of experimental glasses with variable, independently determined CO_2 contents and similar $\text{H}_2\text{O}_{\text{mol}}$ contents to the sample glasses. Such a study is beyond the scope of our work here.

2.5. Calculating Saturation Pressures of Volatiles in Melts

The saturation pressure of fluid in a melt (P_{sat}) refers to the pressure at which the sum of the partial pressures of H_2O and CO_2 in the fluid phase are equal to the confining pressure of the system. We chose to calculate this parameter using the VolatileCalc model (Newman & Lowenstern, 2002), which is considered a reliable means of calculating H_2O – CO_2 solubility in tholeiitic melts with MORB-like alkali concentrations and low CO_2 at pressures <200 MPa (Moore, 2008; Shishkina et al., 2010; Witham et al., 2012). VolatileCalc allows P_{sat} to be calculated using both basaltic and rhyolitic compositional models. As most of the pristine ophiolite glasses have near basaltic compositions, we utilized the basalt model (49 wt% SiO_2). Over the H_2O – CO_2 and temperature range for the ophiolite glasses, however, P_{sat} is relatively insensitive to temperature and SiO_2 concentration, with the end-member basalt and rhyolite solubility models converging to within the precision of FTIR (Dixon, 1997). This suggests that any P_{sat} errors resulting from differences between

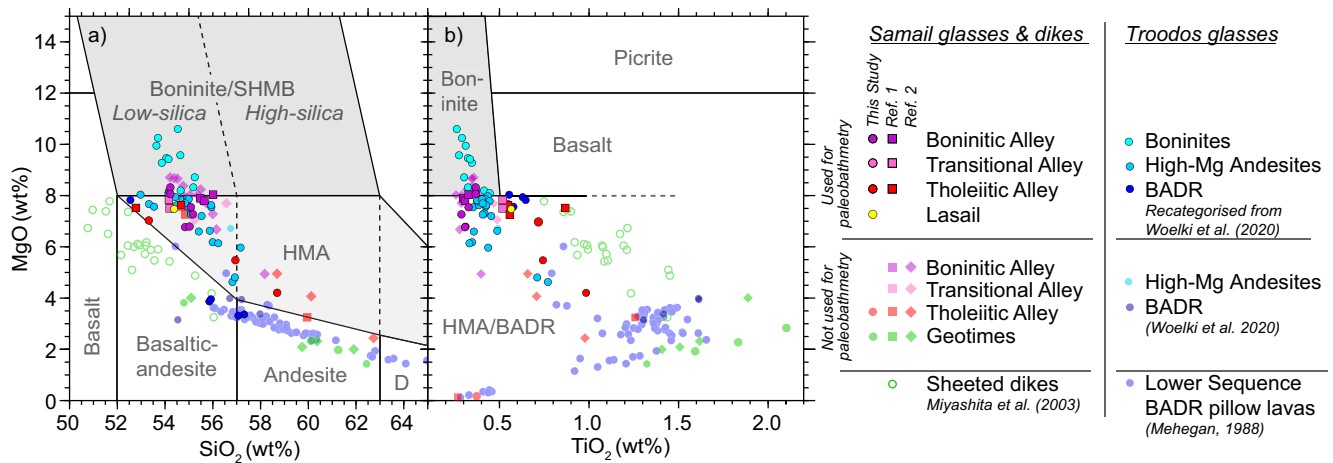


Figure 5. Boninite discriminant diagrams (Pearce & Reagan, 2019) with fields for low and high-Si boninite, high-Mg andesite, siliceous high-Mg basalt, and basalt–andesite–dacite (D)–rhyolite series. (a) SiO₂ versus MgO (b) MgO versus TiO₂. Samail ophiolite glasses: This study; ref. 1 (Belgrano et al., 2019); ref. 2 (Kusano et al., 2017). Additional fresh Samail sheeted dikes from Miyashita et al. (2003). Troodos ophiolite glasses from Woelki et al. (2020) and Group A, Lower Sequence in Mehegan (1988), redescribed by Pearce and Robinson (2010). Pristine glasses with volatile determinations used for paleobathymetry are shown in strong colors; hydrated glasses or those with unmeasured volatile contents are shown in pale colors and not used further. Plotted on an anhydrous basis.

the ophiolite glass and model compositions are minimal. Moreover, our empirically calibrated approach to determining eruption depths should account for any remaining discrepancy.

The mean H₂O and, where available, CO₂ contents for each glass were used to calculate P_{sat} . For the majority of glasses with CO₂ below detection, P_{sat} was calculated for both the CO₂-free and CO₂ = LOD (50 μg/g) cases, yielding a permissible range in P_{sat} for those samples. Eruption temperatures for the Samail and Troodos datasets were calculated using an empirically calibrated geothermometer based on the major element and H₂O composition of each glass sample (Equation 14 in Putirka, 2008). Pressure was converted into ocean depths using a Mid-Cretaceous Tethyan seawater density of 1,026 kg/m⁻³ (Hay, 2009).

3. Results

3.1. Major Element Compositions of Glasses

The Mg–Si–Ti systematics of the Samail and Troodos glasses can be used to better understand their volcanostratigraphic affiliation and categorize them into groups for bathymetric comparison (Figure 5; Pearce & Reagan, 2019). Published glass analyses are shown in Figure 5 for comparison, as well as a relatively fresh subset of Samail sheeted dike compositions (Miyashita et al., 2003).

The Samail Geotimes and sheeted dike data share a BADR fractionation path, supporting the well-established comagmatic relationship of these units (Figure 5a; see also Pearce et al., 1981; Umino et al., 1990). Peak TiO₂ contents occur at ~2.1 wt% TiO₂ and ~3–4 wt% MgO, which fits with previously modelled fractionation trends for Geotimes melts in the presence of 0.5 wt% H₂O (MacLeod et al., 2013). The Tholeiitic Alley glasses trace a scattered fractionation path from the basalt/basaltic-andesite/boninite junction through the high-Mg andesite field into the dacite field (Figure 5a). A range of Tholeiitic Alley compositions, extending from Geotimes-like through to Boninitic Alley and encompassing Transitional Alley are apparent, as reflected in their span of immobile element compositions (Belgrano et al., 2019). The expanded data set further confirms a low-silica boninite parental melt for the Boninitic Alley lavas (Belgrano et al., 2019; Ishikawa et al., 2002; Kusano et al., 2017).

Compositional groups of glasses from the Troodos ophiolite overlap closely with their Samail counterparts (Figure 5). The Troodos lower pillow lavas follow a BADR fractionation path similar to Geotimes, but peak at lower TiO₂ contents of ~1.6 wt% at 2.5–3.5 wt% MgO (Mehegan, 1988; Pearce & Robinson, 2010). Woelki et al. (2020) divided the glasses into boninites and tholeiites based on the Le Bas (2000) classification. For

the purposes of this study, it was useful to re-categorize the Troodos “tholeiites” into BADR-series tholeiites and boninite-series high-Mg andesites, comparable to the Pearce and Robinson (2010) and Samail ophiolite categories.

3.2. Volatile Compositions

In the Samail samples, the mean H₂O concentration in the pristine Alley group glasses is 2.2 wt% ($1\sigma = 0.3$, $n = 16$) and ranges from 1.8–2.7 wt%. The single pristine Axial Lasail glass recovered from the top of the Samail axial sequence has 1.5 ± 0.1 wt% H₂O. There are no significant differences between Tholeiitic Alley glasses, with mean H₂O of 2.2 wt% ($1\sigma = 0.2$, $n = 4$), Transitional Alley glasses with a mean of 2.3 wt% ($n = 2$), and Boninitic Alley glasses, with a mean of 2.1 wt% ($1\sigma = 0.2$, $n = 9$). Just four of the 17 pristine Samail glasses have CO₂ concentrations above the approximate LOD of 50 $\mu\text{g/g}$, and range from 53–82 $\mu\text{g/g}$. The modelled concentrations for the remainder range from 2–46 $\mu\text{g/g}$ but are considered to be potentially unreliable and only utilized as a permissible range of 0–50 $\mu\text{g/g}$ (see Section 2.4.2).

The mean H₂O concentration in all of the pristine Troodos glasses is 2.3 wt% ($1\sigma = 0.2$) with a range of 1.7–2.6 wt% (Woelki et al., 2020). The mean of the Troodos BADR glasses is 2.0 wt% H₂O ($1\sigma = 0.2$, $n = 5$) and the mean of the boninite-series glasses is 2.3 wt% H₂O ($1\sigma = 0.2$, $n = 33$). The disparity in the number of measurements makes a meaningful comparison between the two groups difficult; however, Pearce and Robinson (2010) also noted that H₂O contents in the upper lavas are higher than in the lower lavas. For Troodos, CO₂ determinations were reported for 12 out of the 38 pristine glasses, with a range of 17–104 $\mu\text{g/g}$.

4. Paleobathymetric Interpretation of Volatile Compositions

4.1. Volatile Saturation State

A key assumption of our paleobathymetric approach is that the analyzed glasses formed by quenching of melts that were saturated or supersaturated in a magmatic fluid. There are textural arguments that demonstrate this was the case for both ophiolite sample sets. First, all the studied lavas are, to different extents, vesicular. The commonly globular texture of the sampled lavas in both ophiolites (Figures 2b–2e, see also Belgrano et al., 2019), and isotopic features of these globules, attest to the H₂O-rich nature of this fluid (Ballhaus et al., 2015; Fonseca et al., 2017, 2020). This is further supported by the presence of dendritic quench clinopyroxene in many of the Samail (e.g., Figures 3a and 3b) and Troodos glasses (Fonseca et al., 2017). Such textures form by rapid crystallization induced by H₂O-degassing, which rapidly shifts the liquidus to higher temperatures (Applegarth et al., 2013).

Compositional relationships between H₂O and major element proxies for differentiation (e.g., Si, Mg, K) also allow the H₂O saturation state of the melt during quenching to be assessed (Figure 6). In H₂O-undersaturated melts such as MORB, H₂O behaves incompatibly during fractional crystallization and does not degas at typical ocean ridge seafloor pressures (Danyushevsky et al., 2000; Dixon et al., 1988). The H₂O contents of such lava suites will therefore correlate with proxies for differentiation (e.g., Si, Mg, K). For melts which become H₂O saturated during either ascent or fractional crystallization and which efficiently degas prior to quenching, different products of the same parental melt should erupt with relatively similar, saturated H₂O contents over a range of Si, Mg, and K concentrations. Lastly, melts which reach H₂O saturation during ascent or eruption but do not efficiently degas may become H₂O-supersaturated. In this case, potentially variable degrees of pre-eruptive degassing compounded with variable quenching rates in pillow lavas will lead to variably supersaturated, scattered H₂O contents in the glasses which do not correlate simply with major-element proxies for differentiation (e.g., Escrig et al., 2012; Jenner et al., 2015).

These assessments assume that Si–Mg–K variation within each volcanic unit is predominantly controlled by fractional crystallization. However, parental ratios of these elements vary characteristically between the ophiolite volcanic units (Figure 5a; Belgrano et al., 2019; Kusano et al., 2017; Pearce & Robinson, 2010). Transitional or mixed melts could therefore contribute to some of the scatter in Figure 6, introducing a degree of ambiguity to the assessments.

Nevertheless, pronounced scattering of H₂O between 1.8 and 2.7 wt% over a relatively narrow range of SiO₂ and MgO contents suggests that H₂O was probably supersaturated and had variably degassed from

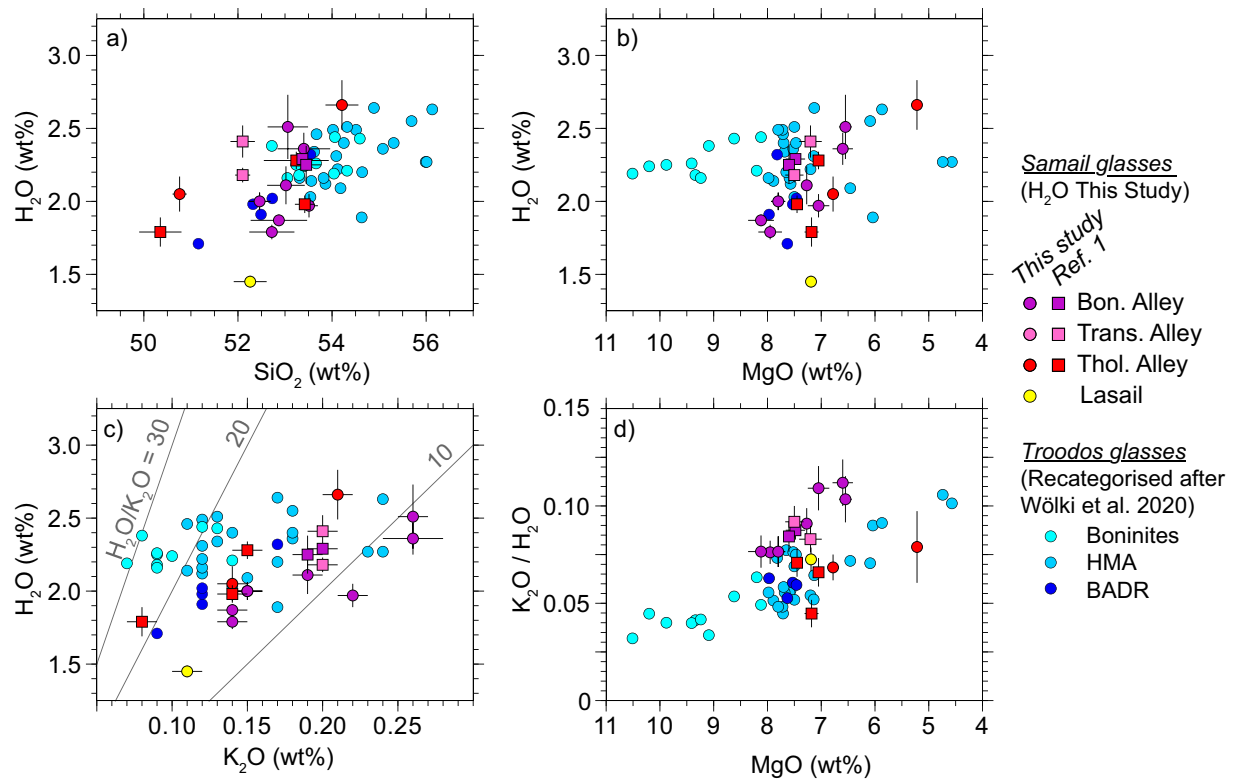


Figure 6. Covariation of H₂O with compatible and incompatible elements in the pristine Samail and Troodos glasses. (a) SiO₂ versus H₂O. (b) MgO versus H₂O. (c) K₂O versus H₂O. (d) MgO versus K₂O/H₂O. Measured, hydrous compositions are plotted. Error bars are 1 σ . Figure 6 compares concentrations of H₂O with those of MgO, SiO₂ and K₂O. Comparison of H₂O concentrations with chemical proxies for magmatic differentiation allows the H₂O saturation state of the melts during quenching to be assessed, as interpreted in the following section.

the Samail Tholeiitic Alley and Boninitic Alley glasses by the time of quenching (Figures 6a and 6b). Contrastingly, the scattered but broadly positive correlation between H₂O and K₂O in the same glasses suggests that the Alley melts were near- or somewhat under-saturated in H₂O during their fractional crystallization and quenching (Figure 6c). As the compatibility of H₂O and K in these melts is similar, K₂O/H₂O ratios should be relatively constant if no H₂O degassing had occurred (Danyushevsky et al., 2000). The scatter in Figure 6d thus supports variable degrees of partial H₂O degassing from the Alley melts prior to quenching.

In the Troodos boninites, H₂O mostly behaved incompatibly with respect to MgO, suggesting it may have been undersaturated or nearly saturated during ascent, fractional crystallization, eruption, and quenching (Figure 6b). The H₂O contents of the high-Mg andesites, however, are spread to lower H₂O contents in a manner consistent with variable degassing of H₂O from a supersaturated state during eruption. Figure 6c shows H₂O is scattered across a range of K₂O contents, which is supportive of H₂O saturation, and the gentle increase of K₂O/H₂O with decreasing MgO could likewise be explained by fractional crystallization at an H₂O content limited by degassing (Figure 6d)

In summary, both ophiolites show geochemical evidence which is supportive of partial H₂O degassing prior to quenching of the sampled glasses. Further, the vesicular and commonly globular textures of the lavas (Figures 2b–2e) and the dendritic quench textures of clinopyroxenes all indicate that the Samail Alley and Troodos pillow lavas were degassing an H₂O-rich magmatic fluid during eruption on the seafloor.

The shift from CO₂ to H₂O dominated degassing only occurs once CO₂ has almost completely degassed, to concentrations below ~100 μ g/g for a closed system or ~10 μ g/g for an open system (Figure 7a), as modelled by Newman and Lowenstern (2002). As seafloor degassing is an open-system process, the above evidence

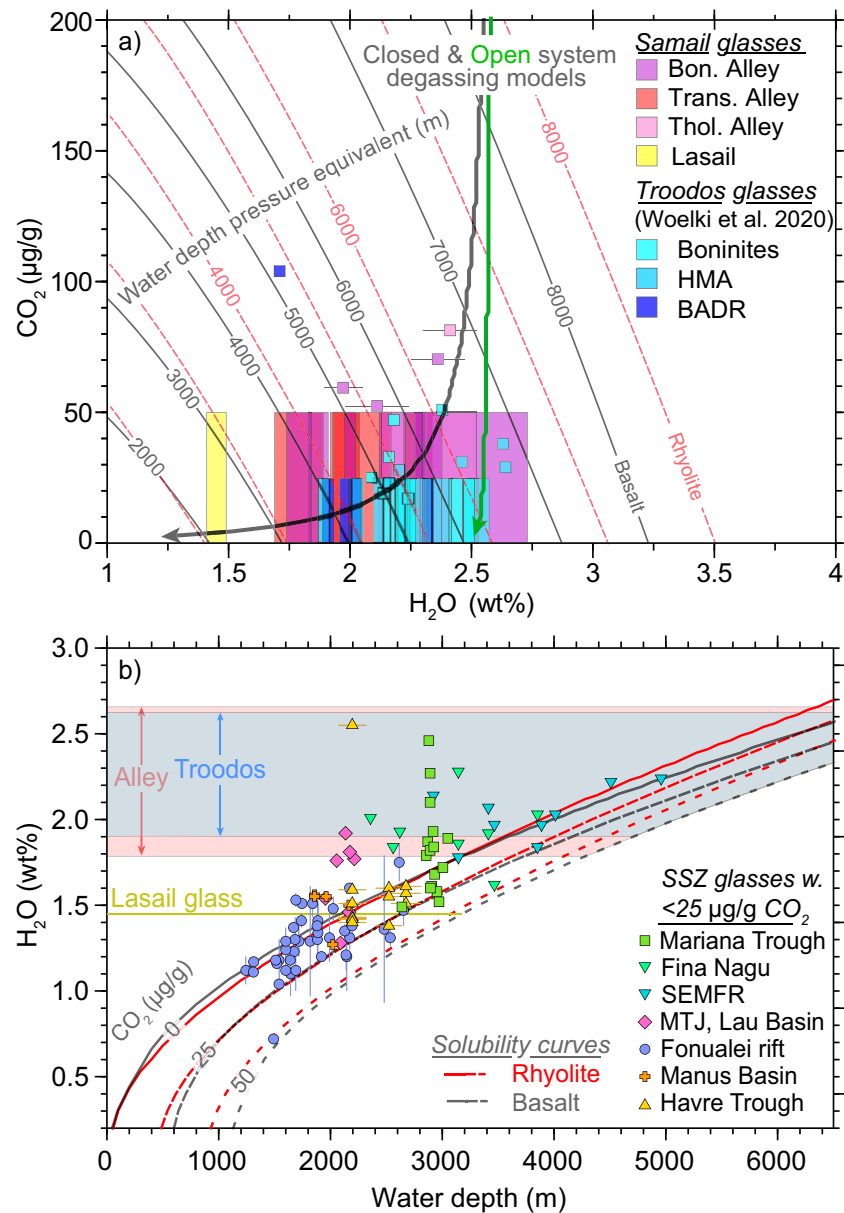


Figure 7. Previous diagrams for assessing eruption depths from the concentrations of volatiles dissolved in volcanic glass. (a) Dissolved H₂O versus CO₂. Boxes for Samail ophiolite glasses (this study) encompass 1 σ for H₂O and the permissible range up to 50 µg/g (limits of detection (LOD)) for CO₂. Boxes for Troodos glasses (Woelki et al., 2020) show measured CO₂ or the permissible range up to 25 µg/g (reported LOD), no H₂O uncertainties were reported. Saturation isobaths calculated in VolatileCalc for basalt (grey lines; 49 wt% SiO₂, 1,200°C) and rhyolite (red dashed lines; 1,000°C) endmembers. Closed and open system degassing path examples modelled in VolatileCalc for a hypothetical parental melt with 2.6 wt% H₂O and 1,000 µg/g CO₂. (b) H₂O versus water depth pressure equivalent. H₂O contents and recovery depths of glasses with CO₂ < 25 µg/g or < FTIR LOD from active supra-subduction zone settings: Mangatolu Triple Junction (Hahm et al., 2012), Fonualei Rift (Escrig et al., 2012; Keller et al., 2008), Southern Mariana Trough (Brounce et al., 2014), Fina Nagu seamount chain (Brounce et al., 2016), Southeast Mariana Forearc Rift (Ribeiro et al., 2015), Manus Basin (Marty et al., 2001), Havre Trough (Wysoczanski et al., 2006). Saturation solubility models plotted with VolatileCalc for both basaltic (49 wt% SiO₂, 1,200°C) and rhyolitic (1,000°C) compositions at 0, 25, and 50 µg/g CO₂.

for H₂O degassing is consistent with the low CO₂ determinations. It follows that the lower values among the range of CO₂ contents are the most significant for estimating the pressure of seawater on the ophiolite glasses.

4.2. Previous Approaches to Volatiles-in-Glass Paleobathymetry

The pressure dependence of H₂O and CO₂ solubility in silicate melts underpins the volatiles-in-glass approach to paleobathymetry (e.g., Dixon & Stolper, 1995; Roberge et al., 2005; Shimizu et al., 2013). The tendency of CO₂-bearing submarine glasses to be somewhat volatile-supersaturated leads to P_{sat} averages which overestimate eruption depths (Dixon & Stolper, 1995; Dixon et al., 1988; Newman et al., 2000).

Figure 7b tests whether supersaturation of H₂O is also common for CO₂-poor suprasubduction zone melts (e.g., Escrig et al., 2012). Supersaturation of H₂O is seldom described for deep submarine glasses as H₂O contents are often compared to a pure-H₂O saturation curve without screening for elevated CO₂ contents. Concentrations of a few tens of $\mu\text{g/g}$ of dissolved CO₂ significantly reduces H₂O solubility and if ignored will make H₂O-oversaturated glasses appear undersaturated.

The H₂O concentrations and recovery depths of glasses with <25 $\mu\text{g/g}$ CO₂ from active supra-subduction zone settings are plotted in Figure 7b. Also shown are volatile saturation curves plotted by VolatileCalc for basalt and rhyolite with 0, 25, and 50 $\mu\text{g/g}$ CO₂. Data lying above the 0 $\mu\text{g/g}$ model must be H₂O-supersaturated, those between the 0 and 25 $\mu\text{g/g}$ curves may be slightly under- or supersaturated, and compositions below the 25 $\mu\text{g/g}$ curve are H₂O-undersaturated. Within uncertainty, most data plot above the 25 $\mu\text{g/g}$ CO₂ curve, and many above the 0 $\mu\text{g/g}$ curve. Therefore, just as for CO₂-rich magmatic fluids in subduction-unrelated settings, supersaturation of H₂O-rich fluids is apparently common in suprasubduction zone settings. Using a P_{sat} calculated from average H₂O values to calculate an eruption depth from the saturation curves would obviously overestimate the true depth (e.g., Woelki et al., 2020). Instead, the lowest H₂O values of the CO₂-poor glass suites yield approximately correct water depths, corresponding to estimates of 3–4 km for the Samail ophiolite and 3.5–4.5 km for the Troodos Ophiolite (Figure 7b).

This approach can be improved by accounting for CO₂ using an H₂O–CO₂ diagram contoured with saturation isobaths (Figure 7a; Dixon & Stolper, 1995). Here, the tendency towards supersaturation means that the shallowest isobaths intersected by a suite of glasses should approximate the eruption depth, suggesting a range of 2.9–4.2 km for the Samail ophiolite and 3.5–4.2 km for the Troodos Ophiolite.

These diagrammatic methods are excellent for assessing degassing paths and give useful first order paleobathymetric estimates. However, they are limited by either their overreliance on the lowest P_{sat} value of a data set or by the subjectivity involved in choosing an appropriately low P_{sat} value. In the next section, we aim to address these shortcomings.

4.3. An Improved Approach to Volatiles-in-Glass Paleobathymetry

Here, we develop an empirically calibrated statistical model for estimating eruption pressures from the P_{sat} distributions of submarine volcanic glass suites and test it on extant, natural examples.

4.3.1. Calibration

The aim of this calibration is to determine a simple summary statistic that can be used to predict eruption depths from the P_{sat} distributions of natural volcanic glass suites. To achieve this, we compiled analyses of glasses with both H₂O and CO₂ determinations from PETDB and published sources. All these glasses had been collected at known ocean depths in volcanically active, intra-oceanic suprasubduction zone settings: back-arc rifts of the Havre Trough (Wysoczanski et al., 2006), the Mariana Trough (Newman et al., 2000), the Manus Basin (Marty et al., 2001), and the Lau Basin (Hahm et al., 2012; Lytle et al., 2012), and the South Eastern Mariana Forearc (SEMFR; Ribeiro et al., 2015). We discarded the data on any samples that appeared to have been collected from old or tectonically disrupted crust. The final data set ($n = 125$) was split by SiO₂ contents into basalt, basaltic-andesite, and andesite categories and these were respectively assigned eruption temperatures of 1,200, 1,100, and 1,000°C. The VolatileCalc basalt model was then used to calculate a P_{sat} for each glass. This compilation as well as the discarded values are archived together with our new data.

The data set was normalized by calculating the percent deviation of the calculated P_{sat} from the known seafloor pressure at each glass recovery site (P_{recovery} ; Figure 8a). The P_{sat} deviation distribution has a single mode at +17% and is skewed toward negative values, in line with previous assessments of MORB and back-arc glass suites (e.g., Dixon et al., 1988; Newman et al., 2000; Shimizu et al., 2013). However, 15% of the

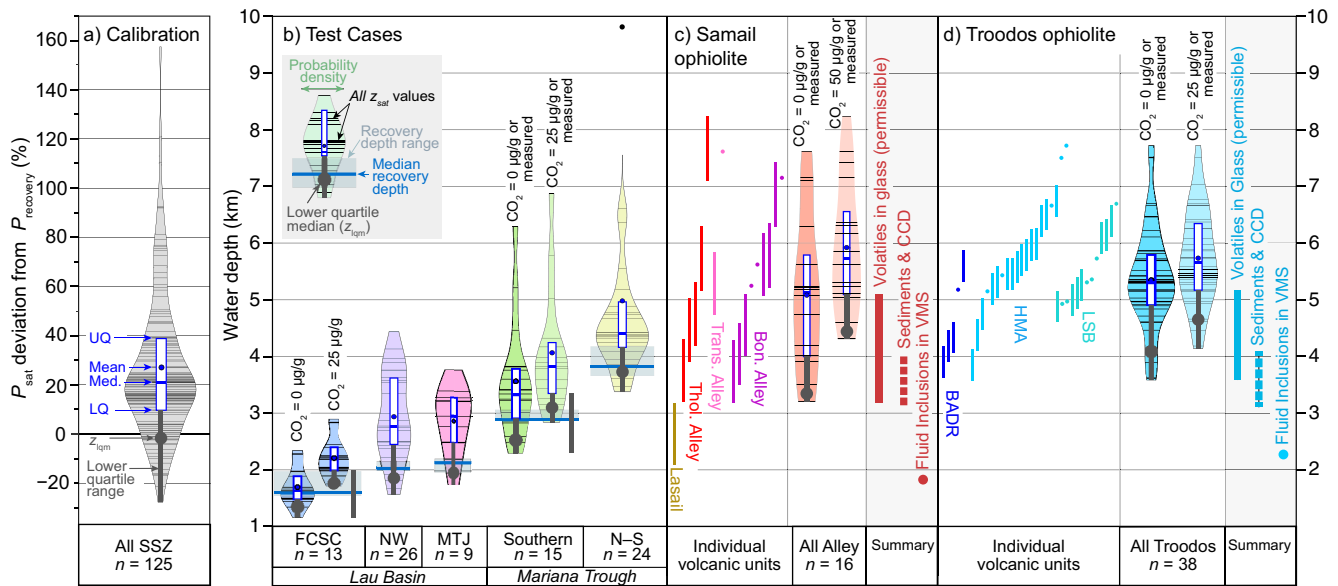


Figure 8. Calibration, testing and prediction of eruptive depths from volcanic glasses. Saturation pressure (P_{sat}) deviation and depth (z_{sat}) distributions plotted as violin (mirrored kernel density) and box plots (a) All supra-subduction zone calibration data set normalized as P_{sat} % deviation from P_{recovery} for West Pacific fore- and back-arc glasses (see Section 4.3.1 for sources and details). (b) Test cases for the lower quartile range and z_{iqm} preferred depth predictions. Lau Basin: Fonualei Central Spreading Centre (Escrig et al., 2012; Keller et al., 2008); North West Lau (Lytle et al., 2012); Mangatolu Triple Junction (Hahm et al., 2012). Mariana Trough: Southern Mariana Trough (Brounce et al., 2014); Northern to Southern (N-S) Mariana Trough (Newman et al., 2000) (c) Samail ophiolite: permissible z_{sat} range for each pristine glass sample (Individual volcanic units); Violin and boxplot distribution of z_{sat} for “All Alley” glasses, with lower quartile range and z_{iqm} used for paleobathymetry (grey bar and dot respectively); “Summary” comparison of glass (this study), sedimentary, and VMS fluid inclusion data. (d) As for (c) but for the Troodos ophiolite: with z_{sat} calculated for each pristine glass in Woelki et al. (2020). Violin plots were created in R with ggplot2 (Wickham, 2016).

data have negative P_{sat} deviations, which is surprising, as volatiles should not degas to concentrations below their solubility. Assuming that these arc-related melts were saturated in a fluid phase, and that the solubility model is reasonably accurate (see Section 2.5), the simplest explanation is that, following their eruption and prior to being collected, the samples with negative deviations had been transported to greater depths in lava flows or debris flows. The implication is that any summary statistic calibrated for predicting eruption depths from this data set should fall below, rather than at, the zero baseline in Figure 8a.

To encompass the two endmember possibilities, first that the published recovery depths equal the true eruption depths and the solubility model is inaccurate for these compositions, and second that some of the glasses have been transported downslope, we take the lower quartile of the entire P_{sat} distribution as a permissible range for predicting eruption depths. For many applications, it is important to have a single preferred prediction together with this permissible range. For this purpose, the median of the lower quartile values (z_{iqm}) is simple to calculate and relatively resistant to data outliers.

4.3.2. Test Cases

To assess the reliability of our predictive model, we applied it to five test cases, each a genetically related suite of glasses collected from a supra-subduction setting (Figure 8b). Groups of glasses were selected from each study based on their recovery from the same tectonic feature over a relatively narrow depth range, and the calculated P_{sat} distributions were converted into seawater depth equivalents (z_{sat}). No data were discarded from these test cases. This contrasts with Figure 7b, where only low- CO_2 glasses are plotted, and with the “All supra-subduction zone” calibration data set, where samples were screened for post-eruption displacement.

The NW Lau (Lytle et al., 2012), Mangatolu Triple Junction (Hahm et al., 2012), and Mariana Trough (Newman et al., 2000) data are also utilized in the calibration data set, which is admittedly circular reasoning, but these tests still serve to demonstrate the internal consistency and applicability of the model to smaller glass suites.

The Fonualei Central Spreading Centre (FCSC; Escrig et al., 2012; Keller et al., 2008) and Southern Mariana Trough (Brounce et al., 2014) test cases were not used for calibration as CO₂ was measured by FTIR and was mostly below detection. These cases serve as independent validations of our approach. As for the ophiolite samples, end-member predictions for these cases were made for distributions calculated with CO₂ concentration equal to zero or the measured value on the one hand, or with CO₂ concentration equal to the measured value or an upper limit on the other. These two predictions are assumed to bracket the true value. The upper limit for CO₂ was fixed at 25 μg/g based on sub-50 μg/g values reported in Brounce et al. (2014), and the clear geochemical evidence for H₂O degassing in the relatively shallow FCSC glasses (Escrig et al., 2012; Keller et al., 2008).

For all five test cases, which have median recovery depths ranging from 1.6 up to 3.8 km, the permissible range predicted by our model (the lower quartile range) correctly encompasses the median and range of the recovery depths for each test case (Figure 8b). As expected, the preferred depth, z_{lqm} (the lower quartile median), is a few percent shallower than the median recovery depth, accounting for some downslope transport from the eruption site. These successful predictions demonstrate the accuracy of our paleobathymetric predictions to within a few hundred meters for sample sets with $n \geq 9$, over a range of different settings, depths, glass compositions, and P_{sat} distributions.

4.3.3. Seafloor Depths During Eruption of the Samail and Troodos Lavas

For both ophiolites, the z_{sat} range calculated from H₂O and either the measured or permissible range of CO₂ concentrations is plotted in Figures 8c and 8d for each glass, organized on a geochemical or stratigraphic unit basis. Beside these, summary distributions are plotted for each ophiolite for assessing seafloor depths. As for the FCSC and S. Mariana Trough test data, the true z_{sat} range for each ophiolite is unknown but bracketed by two distributions plotted for both CO₂ = 0 or measured and CO₂ = LOD or measured. The range of eruption depths predicted both within and between each end-member distribution represents a potential combination of model uncertainty and seafloor topography but cannot be unequivocally ascribed to either.

For the Samail volcanic units (Figure 8c), the single pristine glass from the axial magmatic stage has a permissible z_{sat} range of 2,090–3,190 mbsl, which is shallower than the post-axial Alley glasses, hinting at the possibility of a shallower axial stage. Among the post-axial Alley group glasses, there is no significant difference between the early Tholeiitic Alley or later Boninitic Alley glasses. Accordingly, the entire Alley group is combined into a single data set for estimating post-axial depths of eruption. The permissible range for the Samail post-axial lavas is thus 3,190–5,080 mbsl. For the CO₂ = 0 or measured end member, a permissible range of 3,190–3,990 mbsl and preferred z_{lqm} of 3,350 mbsl are predicted. For the CO₂ = measured or 50 μg/g end member, a permissible range of 4,300–5,080 mbsl and a z_{lqm} 4,450 mbsl are predicted. In the following discussion, we justify a preference for the shallower prediction, but the two z_{lqm} values can be averaged into a single prediction and total uncertainty of 3900_{-710}^{+1190} mbsl.

There are no clear differences between the z_{sat} distributions of the Troodos glass compositional groupings (Figure 8d). As such, the entire Troodos pristine glass data set is used in the summary distribution. The permissible range of eruption depths for the Troodos lavas is thus 3,580–5,170 mbsl. For the low CO₂ end-member, a permissible range of 3,580–4,910 mbsl and a preferred z_{lqm} of 4,108 mbsl are predicted. For the CO₂ = 25 μg/g or measured endmember, a permissible range of 4,140–5,170 mbsl and preferred z_{lqm} 4,660 mbsl are predicted. The two z_{lqm} values can be averaged into a single prediction and total uncertainty of 4380_{-800}^{+790} mbsl. This overlaps with the ~5 km estimate made by Woelki et al. (2020) on the basis of the average H₂O concentration, however for reasons outlined in the following discussion, the shallower end of the permissible range is preferred.

5. Discussion

5.1. Comparison With Sedimentary Evidence

The presence or absence of biogenic carbonate in ophiolite sediments can be related to ocean depth via reconstructions of past CCD. Cretaceous reconstructions exist for the Indian, Atlantic and Pacific oceans (Figure 9a; Sclater et al., 1977; Van Andel, 1975). For the times that the Samail and Troodos crust formed,

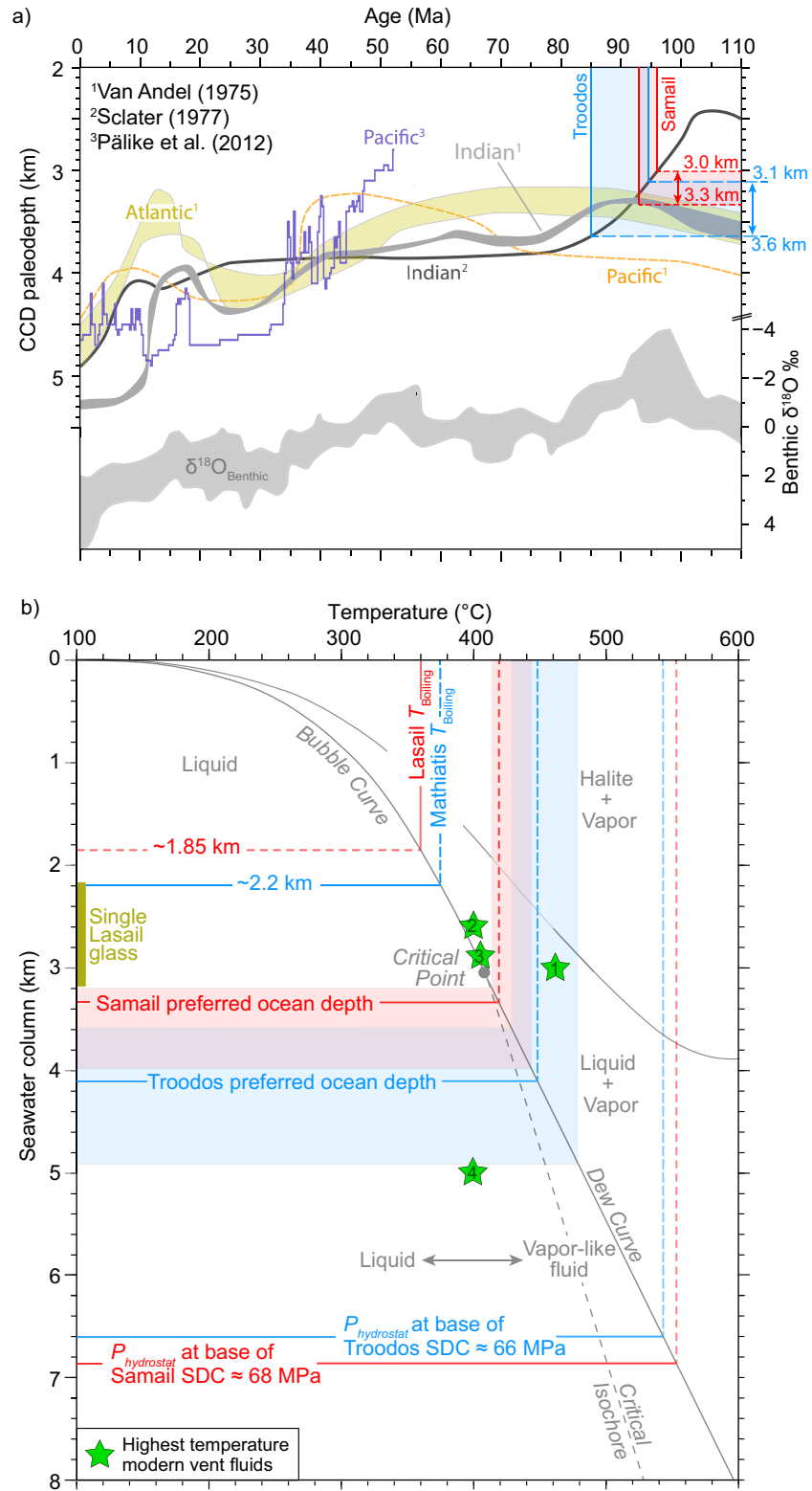


Figure 9

these reconstructions record a relatively shallow range of global CCDs between 3.0–3.9 km, with the Indian Ocean, which adjoined the now-closed Neo-Tethys, being slightly shallower at 3.0–3.7 km (Figure 9a). More recent, high resolution CCD reconstructions for the Cenozoic Pacific demonstrate that short term, high amplitude fluctuations can be superimposed over the secular variations recorded by the 1970s reconstructions (Pälike et al., 2012). The CCD is also broadly correlated with benthic $\delta^{18}\text{O}$, a proxy for ocean temperature (Pälike et al., 2012). The formation of the Samail and Troodos crust coincides with a period of rapid decline from the highest benthic $\delta^{18}\text{O}$ on record (Friedrich et al., 2012), suggesting the CCD was deepening as the crust formed (Figure 9a). Together with the differences between CCD reconstructions for the Indian Ocean during the Cretaceous, these factors suggest that the CCD should be considered with at least ± 0.5 km uncertainty.

5.1.1. Samail Ophiolite

Inter-lava sediment layers consisting of ferromanganous mudstones, cherts and umbers are common within the 2–3 km thick Samail volcanic sequence, and in almost all cases are devoid of pelagic carbonate. The exceptions are the rare calcareous mudstones in the top few hundreds of meters of the volcanic pile in the Fizeh and Salahi blocks (Figure 2f; Belgrano et al., 2019; Robertson & Fleet, 1986). The Suhaylah Formation overlying the Samail volcanic sequence consists of umbers which grade upwards into several meters of typically carbonate-poor radiolarian mudstones and cherts, before transitioning further upsection into micritic limestone (Figure 2g; Robertson & Fleet, 1986). We have observed that in the rare areas where calcareous sediments occur within the uppermost lavas, calcareous mudstones also directly overlie the basal umbers of the Suhaylah formation (e.g., Wadi Rajmi).

Fleet and Robertson (1980) and Robertson and Fleet (1986) argued that these locally calcareous sediments indicate that volcanism occurred entirely above the CCD horizon. Carbonate dissolution by acidic hydrothermal fluids and the overwhelming of carbonate-forming organisms by radiolaria, promoted by hydrothermal venting of silica, were offered as potential explanations for the predominance of siliceous sediments. The conformable and paleontologically defined gradation of the Suhaylah unit is not suggestive of hydrothermal dissolution of carbonates in the lower subunit (Figure 2g; Hara & Kurihara, 2017). Moreover, studies of the modern Southwest Indian Ridge, which is shallower than the CCD, show that pelagic carbonate sediment continues to accumulate even where metalliferous sediments are depositing near hydrothermal vents (Pan et al., 2018). Concerning the idea that carbonate-forming organisms would be suppressed by hydrothermal silica, this would have to occur throughout the entire water column to explain the absence of seafloor carbonate. This seems improbable given that silica enrichment in modern vent-distal hydrothermal plumes is modest and does not extend above mid-ocean depths (Johnson et al., 2006; Mortlock et al., 1993).

The above observations indicate that the Samail lavas erupted mostly just below the CCD horizon, which was in the region of 3.0–3.3 km (Figure 9a), and that the latest boninite accumulations locally protruded above the CCD. This sedimentary evidence fits well with our endmember depth estimate based on CO_2 -poor volatiles in glass, which is also supported by the evidence for H_2O degassing (see Section 4.1), pointing to ocean depths somewhere between 3.2 and 4.0 km during Samail volcanism (Figure 8c).

Figure 9. Alternative paleobathymetric evidence. (a) Carbonate compensation depth (CCD) reconstructions since 110 Ma for the Indian, Pacific, and Atlantic oceans (Pälike et al., 2012; Sclater et al., 1977; Van Andel, 1975). Benthic $\delta^{18}\text{O}$ compilation, a proxy for ocean temperature (Friedrich et al., 2012), for comparison with the CCD reconstructions. (b) Seawater (3.2 wt% NaCl) phase diagram after Driesner and Heinrich (2007), with pressure converted to depth equivalent. The intersection of independently determined temperatures or depths (solid lines) with the bubble curve (at $T < T_{\text{critical}}$) or dew curve (at $T > T_{\text{critical}}$) can be related to a depth or temperature via the dashed orthogonal lines. The preferred depth (z_{iqm}) and lower quartile ranges (shaded) for the low- CO_2 volatile in glass z_{sat} distributions are shown. Boiling temperature for the Lasail volcanogenic massive sulfide (VMS) deposit, situated at the top of the Samail axial lavas, is estimated from Spooner and Bray (1985). Boiling pressure for the Mathiatis VMS deposit, situated at the Troodos Lower–Upper Pillow lava contact, is from Spooner (1980). Cold hydrostatic pressures ($P_{\text{hydrostat}}$) at the base of the sheeted dike complex are approximated by adding the typical thickness of the entire upper crust (Figure 1) to the preferred z_{iqm} estimates of lava eruption depth, assuming a constant seawater density of $1,026 \text{ kg/m}^3$. Green stars are examples of high temperature submarine vent fluids: (1) Mid-Atlantic Ridge, 5°S , transiently reached 464°C (Koschinsky et al., 2008) (2) East Pacific Rise, 9°N (Von Damm et al., 1995); (3) East Pacific Rise, 21°S (Von Damm et al., 2003); (4) Beebe vent field, Cayman Trough (Webber et al., 2015).

5.1.2. Troodos Ophiolite

The intra-lava sediments of the Troodos ophiolite similarly consist of umbers and metalliferous mudstones and cherts. Fossils in the Troodos intra-lava sediments are predominantly radiolarian and equivocally biogenic carbonate is rare, leading many authors to suggest eruption depths deeper than the CCD (Cann & Gillis, 2004; Robertson, 1975; Robertson & Hudson, 1974). Similarly, however, to the Samail ophiolite, the occurrence of rare carbonate fossils has been used to contend that the Troodos seafloor was shallower than the CCD (Boyle, 1990; Boyle & Robertson, 1984; Robertson, 2004; Robertson et al., 1991). These arguments hinge on descriptions of trace carbonate fossils in intra-lava sediments by Mantis (1971) and Boyle (1984). Mantis (1971) described Campanian benthic foraminifera in a drill core sample, and Boyle's (1984) original observations describe abundant ostracods but just one coccolith and one sample with planktonic foraminifera.

We argue that this trace fossil evidence does not necessarily situate the Troodos seafloor shallower than the CCD. First, trace carbonate may be preserved deeper than the modern CCD (Pälike et al., 2012). Indeed, the cutoff used by Van Andel (1975) to define the CCD is <20 wt% CaCO_3 in the sediments. Additionally, it has since been shown that ostracods can thrive below the CCD (Brandão et al., 2019). Occasional foraminifera in otherwise radiolarian sediments are better explained by Boyle's (1984) original proposal that the Troodos seafloor lay somewhat deeper than the CCD, but that final dissolution of sedimenting carbonate occurred on the seafloor rather than within the overlying seawater column. Rapid burial by new lavas would then isolate some fossils and halt dissolution. All this fits with the absence of carbonate fossils in the supra-ophiolitic Perapedhi Formation, where no subsequent lavas were erupted to halt dissolution (Cann & Gillis, 2004; Robertson, 1975; Urquhart & Banner, 1994).

In summary, this sedimentary evidence suggests that Troodos volcanism took place below but in the vicinity of the CCD, which was in the region of 3.1–3.6 km below sea level (Figure 9a). This conclusion is consistent with the range permitted by glass compositions (Figure 8d). Boyle's (1984) interpretation that the seafloor lay just below the CCD horizon lends weight to the shallower, low- CO_2 volatile-in-glass prediction, which is also supported by the evidence for H_2O degassing (see Section 4.1), and corresponds to a permissible range between 3.6 and 4.9 km, with a preferred depth of 4.1 km. The broad range of depth estimates shown in Figure 8d, as well as their long tail toward shallower depths, could be partly attributed to seafloor topography, which was up to 500–800 m across syn-volcanic horst and graben structures (Ella, 2014).

5.2. Comparison With Fluid Inclusion Evidence

Fluid inclusions in hydrothermal minerals record the density, composition and phase-state of the ambient fluids during mineral growth or mineral deformation. Inclusions that form during mineral growth (primary inclusions) can be distinguished from later secondary inclusions by petrographic relationships, best viewed in cathodoluminescence imaging. Groups of coeval fluid inclusions (“fluid inclusion assemblages”) with variable liquid/vapor proportions are interpreted to have trapped random mixtures of immiscible liquid and vapor (Diamond, 2003; Roedder, 1984). Such assemblages commonly form at seafloor vents when the discharging fluid is boiling. The standard approach to derive the temperature of fluid trapping (T_{trap}), is to first screen the assemblages using petrographic criteria for post-entrapment modifications then take the lowest homogenization temperature (T_{h}) measured in the assemblage as representing T_{trap} of the two-phase fluid mixture. Knowing T_{trap} in turn allows the trapping pressure (P_{trap}) to be deduced precisely by intersection with the relevant experimentally determined bubble curve or dew curve (Figure 9b; Diamond, 2003; Roedder, 1984). Only one incompletely documented description of liquid + vapor entrapment in fluid inclusions from a fossil seafloor vent site (VMS deposit) is available for each of the Samail and Troodos ophiolites.

5.2.1. Samail Ophiolite

Spooner and Bray (1985) reported the occurrence of primary, aqueous inclusions with variable liquid/vapor ratios in stockwork quartz below the Lasail VMS deposit, which sits at the contact between Geotimes axial lavas and Tholeiitic Alley post-axial lavas (Gilgen et al., 2014). Their publication is a brief conference abstract, thus it contains neither illustrations nor detailed descriptions. The apparently coexisting liquid-rich and vapor-rich inclusions have salinities of 3.5–8.6 wt% $\text{NaCl}_{\text{equiv}}$ and T_{h} of 360–400°C. Assuming the modal T_{h} to equal T_{trap} , Spooner and Bray (1985) deduced a fluid pressure during boiling of ~ 230 bar, equivalent

to an ocean depth of 2.3 km. We instead apply the standard approach described above and equate the minimum T_h of $\sim 360^\circ\text{C}$ with T_{trap} , arriving at a depth of ~ 1.85 km via the seawater bubble curve (Figure 9b).

This is considerably shallower than the depths of 3 km or more deduced from the volatiles-in-glass and CCD evidence for the Samail ophiolite (Figure 8c). Normal cooling-related subsidence of the seafloor on the order of 250–450 m is plausible during the ~ 1 Myr period between the peaks of axial and post-axial volcanism (Korenaga & Korenaga, 2008; Rioux et al., 2021). This still leaves a discrepancy of 0.5–1 km or more between the fluid inclusion results and those of the other methods. The balance of evidence thus weighs against the fluid inclusion interpretation of Spooner and Bray (1985). It is conceivable that the inclusions were in fact secondary rather than primary, or that the variable liquid/vapor proportions were due to post-entrapment necking down (Roedder, 1984). Both possibilities may be difficult to recognize without modern petrographic equipment.

5.2.2. Troodos Ophiolite

The ocean depth during volcanism in the Troodos ophiolite was estimated at 2.5 ± 0.3 km based on a fluid inclusion study of the Mathiatis VMS stockwork (Spooner, 1980). The Mathiatis deposit is situated at the contact between the Lower and Upper Pillow Lavas (Adamides, 2010). The key textural and microthermometric information necessary to deduce this depth is unfortunately not documented in Spooner (1980). Nevertheless, assuming that the results were treated similarly to the Spooner and Bray (1985) data, the lower limit of the depth estimate (2.2 km) suggests $T_{\text{trap}} \approx 375^\circ\text{C}$, as indicated in Figure 9b.

This discrepancy, whereby fluid inclusions indicate water depths >1 km shallower than the other lines of evidence, is remarkably similar to that deduced above for the Samail ophiolite. This similarity perhaps suggests an unconsidered conceptual flaw in the comparison, or otherwise, dramatic seafloor subsidence between the early and late volcanic stages. However, it is also similarly conceivable that the key Mathiatis inclusions were not primary or that post-entrapment necking down scattered their liquid/vapor proportions. With such sparse and, again, incomplete fluid inclusion evidence, the volatiles-in-glass evidence that we have presented rather points to ocean depths in excess of 3.6 km for the Troodos ophiolite.

5.3. Implications for the Tectonic Setting of Ophiolite Formation

The preferred water depths indicated by our results, of ~ 3.4 km for the Samail ophiolite and ~ 4.1 km for the Troodos ophiolite, are considerably deeper than the typical axial depths of most structurally comparable mid-ocean or back-arc ridges (Monecke et al., 2014; Small, 1994). The proposed depths, however, do overlap with the recovery depths for fore-arc tholeiites in the South East Mariana Forearc (3–5 km, Figure 7b; Ribeiro et al., 2015), and with compositionally similar low-Ti arc tholeiites and boninites recovered from the trenchward side of the Matthew–Hunter subduction initiation terrane (3–5 km; Patriat et al., 2019). Our results are thus supportive of either the proto-arc (i.e., subduction initiation) or fore-arc spreading tectonic models put forward for the Troodos (e.g., Pearce & Robinson, 2010; Robinson et al., 1983; Woelki et al., 2020) and Samail ophiolites (e.g., Belgrano & Diamond, 2019; Guilmette et al., 2018; MacLeod et al., 2013). Further work on the archetypal Izu-Bonin-Mariana proto-arc will elucidate whether >3.4 km water depths are typical for subduction initiation volcanic terranes.

5.4. Implications for Hydrothermal Systems

The seafloor hydrostatic pressures indicated by our results are 10–20 MPa greater than those of typical modern back-arc and mid-ocean ridges (Humphris & Klein, 2018; Monecke et al., 2014) and of those previously assumed in studies of hydrothermal systems in the ophiolites (e.g., Nehlig et al., 1994; Quandt et al., 2018).

5.4.1. High Pressure Hydrothermal Conditions

Hydrostatic pressure fundamentally influences oceanic hydrothermal systems by controlling, among other factors, the temperature of fluid phase transitions, the density of fluids, and the salinity of the products of liquid–vapor separation (Bischoff & Pitzer, 1989). Our estimated hydrostatic pressures at the Samail and Troodos seafloors exceed the critical pressure of seawater (30.1 MPa; Figure 9b) and hence they would have precluded boiling of hydrothermal fluids prior to or upon venting. Assuming cold hydrostatic fluid

pressures within downflow zones in the ~3.5 km thick Samail upper crust, an estimated seafloor depth of ~3.4 km corresponds to a fluid pressure at the base of the relatively permeable sheeted dyke complex of ~68 MPa (total hydrostatic pressure would be somewhat reduced for a column of hot, less dense hydrothermal fluids in an upflow zone). Similarly, for the Troodos ophiolite, our preferred seafloor depth of ~4.1 km implies ~66 MPa at the base of the ~2.5 km thick upper crust (Figure 9b). This permits single-phase fluid to be stable up to temperatures of ~540 and 555°C before potentially intersecting the dew curve in the Troodos and Samail sheeted dike complexes, respectively (Figure 9b). At such high pressures and temperatures, any vapor-like fluid that does intersect the dew curve due to heating or decompression would condense a small amount of brine that is much more saline than if the phases separated closer to the critical point, thus leaving the vapor depleted in salt. Transient venting of fluids with half the salinity of seawater at up to 464°C on the Mid-Atlantic Ridge (star 1 in Figure 9b; Koschinsky et al., 2008) testifies to this process.

It also seems likely that convecting fluids in high pressure ocean-ridge hydrothermal systems will attain higher peak temperatures than in lower pressure systems that are otherwise equivalent. This is based on the hypothesis that the effect of pressure on fluid density, viscosity, and enthalpy induces downwelling fluids to attain a characteristic temperature, corresponding to the peak in fluxibility, before ascending (Jupp & Schultz, 2000, 2004). Simulations based on pure water predict that for otherwise identical hydrothermal systems, hydrostatic pressures of 20, 40 and 60 MPa correspond to respective peak fluxibility temperatures of approximately 380, 450, and 550°C (Jupp & Schultz, 2000, 2004). Fluids of seawater salinity will attain even higher temperatures (i.e., on the order of 30°C more; Jupp & Schultz, 2000).

Whether natural systems do in fact operate like this is still open. However, the hypothesis is supported by the observation that vent fluids at the East Pacific Rise (2–3 km ocean depth) characteristically approach but never significantly exceed the peak fluxibility temperature of around 400°C (e.g., stars 2 and 3 in Figure 9b; Jupp & Schultz, 2000). The observation of 401°C vent fluids that record chemical signatures of deep sub-surface equilibration temperatures of around 500°C at the Piccard vent field, situated at 4.97 km ocean depth, further supports this hypothesis (star 4 in Figure 9b; McDermott et al., 2018; Webber et al., 2015).

If it is true that the peak temperature of ocean ridge hydrothermal cells corresponds to the peak fluxibility temperature, then downwelling fluids in the Semail and Troodos hydrothermal systems should have attained peak temperatures well above 450°C. Such temperatures would have enhanced the capacity of these systems to transport heat and mass relative to shallower, typical MOR systems. This includes enhanced leaching of the VMS metals Cu, Au, Ag, Zn, Fe and Mn, whose solubility increases almost exponentially with temperature (Bischoff, 1980; Fuchs et al., 2019; Seyfried et al., 1997). As suggested by Woelki et al. (2020), the high pressure conditions in the ophiolite systems may therefore partly explain their higher overall intensities of hydrothermal alteration and larger VMS deposits compared to those documented in modern mid-ocean and back-arc crust (Adamides, 2010; Alt et al., 1998; Gilgen et al., 2014, 2016; Gillis & Banerjee, 2000).

5.4.2. Gold Enrichment in the Samail VMS Deposits

The VMS deposits hosted by Boninitic Alley lavas in the Samail ophiolite have higher gold grades (0.8–3.4 g/t) than deposits in the lower Geotimes and Tholeiitic Alley lavas (0.1–0.2 g/t; Gilgen et al., 2014). The mechanisms behind this gold enrichment remain unclear, but there are three leading hypotheses: primary gold enrichment in the boninite source rocks prior to leaching (e.g., Gilgen et al., 2014; Moss et al., 2001), direct magmatic–hydrothermal additions of gold (e.g., Martin et al., 2020; Patten et al., 2019), and enhanced gold precipitation due to vigorous boiling at shallower vent sites (Fuchs et al., 2019; Gilgen et al., 2014). Our paleobathymetric comparison of the Tholeiitic Alley and Boninitic Alley volcanic units shows that there was no significant change in ocean depth between these two volcanic episodes (Figure 8c), and that in any case, boiling could not have occurred at such high seafloor pressures. This rules out gold enrichment by enhanced vent-site boiling during the Boninitic Alley stage, leaving the remaining hypotheses and the possible effects of brine condensation to be tested.

6. Conclusions

We have developed an improved method for estimating the ocean depth during eruption of ancient submarine lavas, based on the H₂O and CO₂ concentrations in suites of volcanic glasses. Using newly measured and previously published glass compositions, we have deduced a permissible range of eruption depths for the Samail and Troodos ophiolites, and further constrained this range with sedimentary evidence for the relative positions of the seafloor and the marine CCD. Together this evidence constrains the post-axial, syn-volcanic seafloor of the Samail realm to between 3.2 and 4.0 km below sea level, with a preferred depth of ~3.4 km, whereas it constrains the Troodos seafloor to depths between 3.6 and 4.9 km, with a preferred value of ~4.1 km.

These depths are 1–2 km greater than for typical mid-ocean or back-arc spreading axes and than those previously assumed in most studies of the ophiolites. Some pressure-dependent models and calculations will consequently require reassessment. Significantly, the high hydrostatic pressures imposed on the ophiolite hydrothermal systems may have allowed convecting hydrothermal fluids to reach peak temperatures 50–100°C higher than for typical modern ocean ridge systems under ~2.5 km of water.

While FTIR proved an excellent tool for measuring H₂O contents and speciation in the ophiolite glasses, CO₂ was rarely quantifiable. Future efforts to better constrain our paleobathymetric estimates would benefit from an additional method with a lower detection limit for CO₂. Our approach to paleobathymetry leaves further room for improvement through recalibration with glasses collected in situ by submarine vehicles, as well as by the use of more sophisticated volatile solubility and statistical models befitting such calibration data. Nevertheless, it represents the first empirically developed and tested approach to ophiolite paleobathymetry, as well as a significant step forward in objectivity and reproducibility.

Data Availability Statement

All new and newly derived data for the Samail and Troodos ophiolites as well as the test and calibration datasets are deposited at <http://doi.org/10.5281/zenodo.4965176> (Belgrano et al., 2021).

Acknowledgments

We thank Chris Ballhaus and an anonymous reviewer for their constructive reviews, Ed Spooner and Alastair Robertson for their correspondence on the different lines of ophiolite paleobathymetric evidence, and Dominic Woelki and Maryjo Brounce for the initial conversations that led to this work. Polished sections were prepared with great care by Thomas Aebi (University of Bern). Pierre Lanari (University of Bern) and Julian Allaz (ETH Zürich) are gratefully acknowledged for their assistance with EMPA. The Public Authority for Mining, Sultanate of Oman, are thanked for their permission to undertake fieldwork in Oman, and Robin Wolf and Samuel Weber are thanked for their assistance in the field. This research was supported by Swiss National Science Foundation (SNSF) grant no. P2BEP2-191795 to T. M. Belgrano and by SNSF grant no. 200020-169653 to L. W. Diamond.

References

- Adamides, N. G. (2010). Mafic-dominated volcanogenic sulphide deposits in the Troodos ophiolite, Cyprus Part 1 – The deposits of the Solea graben. *Applied Earth Science*, 119(2), 65–77. <https://doi.org/10.1179/1743275811Y.0000000001>
- Alabaster, T., Pearce, J. A., & Malpas, J. (1982). The volcanic stratigraphy and petrogenesis of the Oman ophiolite complex. *Contributions to Mineralogy and Petrology*, 81(3), 168–183. <https://doi.org/10.1007/BF00371294>
- Alt, J. C., Teagle, D. A. H., Brewer, T., Shanks, W. C., & Halliday, A. (1998). Alteration and mineralization of an oceanic forearc and the ophiolite-ocean crust analogy. *Journal of Geophysical Research*, 103(B6), 12365–12380. <https://doi.org/10.1029/98jb00598>
- Applegarth, L. J., Tuffen, H., James, M. R., & Pinkerton, H. (2013). Degassing-driven crystallisation in basalts. *Earth-Science Reviews*, 116, 1–16. <https://doi.org/10.1016/j.earscirev.2012.10.007>
- Ballhaus, C., Fonseca, R. O. C., Munker, C., Kirchenbaur, M., & Zirner, A. (2015). Spheroidal textures in igneous rocks - Textural consequences of H₂O saturation in basaltic melts. *Geochimica et Cosmochimica Acta*, 167, 241–252. <https://doi.org/10.1016/j.gca.2015.07.029>
- Belgrano, T. M., & Diamond, L. W. (2019). Subduction-zone contributions to axial volcanism in the Oman-U.A.E. ophiolite. *Lithosphere*, 11(3), 399–411. <https://doi.org/10.1130/L1045.1>
- Belgrano, T. M., Diamond, L. W., Vogt, Y., Biedermann, A. R., Gilgen, S. A., & Al-Tobi, K. (2019). A revised map of volcanic units in the Oman ophiolite: Insights into the architecture of an oceanic proto-arc volcanic sequence. *Solid Earth*, 10, 1181–1217. <https://doi.org/10.5194/se-10-1181-2019>
- Belgrano, T. M., Tollan, P. M., Marxer, F., & Diamond, L. W. (2021). *Major element and volatile compositions of volcanic glasses and related datasets for paleobathymetry of the Samail & Troodos ophiolites*. Zenodo. <https://doi.org/10.5281/zenodo.4965176>
- Bischoff, J. L. (1980). Geothermal system at 21°N, East Pacific Rise: Physical limits on geothermal fluid and role of adiabatic expansion. *Science*, 207(4438), 1465–1469. <https://doi.org/10.1126/science.207.4438.1465>
- Bischoff, J. L., & Pitzer, K. S. (1989). Liquid-vapor relations for the system NaCl-H₂O: Summary of the P-T-x surface from 300° to 500°C. *American Journal of Science*. <https://doi.org/10.2475/ajs.289.3.217>
- Boyle, J. F. (1984). *The origin and geochemistry of the metalliferous sediments of the Troodos Massif, Cyprus*. University of Edinburgh. Retrieved from <https://www.era.lib.ed.ac.uk/bitstream/1842/7089/1/349198.pdf>
- Boyle, J. F. (1990). The composition and origin of oxide metalliferous sediments from the Troodos ophiolite. In J. Malpas, E. M. Moores, A. Panayiotou, & C. Xenophontos (Eds.), *Ophiolites, oceanic crustal analogues: Proceedings of the Symposium "Troodos 1987"* (pp. 705–718). Nicosia, Cyprus. Geological Survey Department.
- Boyle, J. F., & Robertson, A. H. F. (1984). Evolving metallogenesis at the Troodos spreading axis. *Geological Society, London, Special Publications*, 13(1), 169–181. <https://doi.org/10.1144/GSL.SP.1984.013.01.15>
- Brandão, S. N., Hoppema, M., Kamenev, G. M., Karanovic, I., Riehl, T., Tanaka, H., et al. (2019). Review of Ostracoda (Crustacea) living below the Carbonate Compensation Depth and the deepest record of a calcified ostracod. *Progress in Oceanography*, 178, 102–144. <https://doi.org/10.1016/j.pocean.2019.102144>

- Brounce, M. N., Kelley, K. A., & Cottrell, E. (2014). Variations in $\text{Fe}^{3+}/\Sigma\text{Fe}$ of Mariana Arc Basalts and Mantle Wedge fO_2 . *Journal of Petrology*, 55(12), 2513–2536. <https://doi.org/10.1093/petrology/egu065>
- Brounce, M. N., Kelley, K. A., Stern, R., Martinez, F., & Cottrell, E. (2016). The Fina Nagu volcanic complex: Unusual submarine arc volcanism in the rapidly deforming southern Mariana margin. *Geochemistry, Geophysics, Geosystems*, 17(10), 4078–4091. <https://doi.org/10.1002/2016GC006457>
- Cameron, W. E. (1985). Petrology and origin of primitive lavas from the Troodos ophiolite, Cyprus. *Contributions to Mineralogy and Petrology*, 89(2–3), 239–255. <https://doi.org/10.1007/BF00379457>
- Cann, J., & Gillis, K. (2004). Hydrothermal insights from the Troodos ophiolite, Cyprus. In E. E. Davis, & H. Elderfield (Eds.), *Hydrogeology of the oceanic lithosphere* (pp. 272–310). Cambridge University Press.
- Cyprus Geological Survey Department (1995). *Geological Map of Cyprus 1:250,000*. Nicosia. Geological Survey Department, Ministry of Agriculture, Natural Resources and Environment, Government of Cyprus.
- Danyushevsky, L. V., Eggins, S. M., Falloon, T. J., & Christie, D. M. (2000). H_2O abundance in depleted to moderately enriched mid-ocean ridge magmas; Part I: Incompatible behaviour, implications for mantle storage, and origin of regional variations. *Journal of Petrology*, 41(8), 1329–1364. <https://doi.org/10.1093/petrology/41.8.1329>
- Diamond, L. W. (2003). Systematics of H_2O inclusions. In I. Samson, A. Anderson, & D. Marshall (Eds.), *Fluid inclusions: Analysis and interpretation* (Vol. 32, pp. 55–78). Québec. Mineralogical Association of Canada.
- Dixon, J. E. (1997). Degassing of alkalic basalts. *American Mineralogist*, 82(3–4), 368–378. <https://doi.org/10.2138/am-1997-3-415>
- Dixon, J. E., & Stolper, E. M. (1995). An experimental study of water and carbon dioxide solubilities in mid-ocean ridge basaltic liquids. Part II: Applications to degassing. *Journal of Petrology*, 36(6), 1633–1646. <https://doi.org/10.1093/oxfordjournals.petrology.a037268>
- Dixon, J. E., Stolper, E. M., & Delaney, J. R. (1988). Infrared spectroscopic measurements of CO_2 and H_2O in Juan de Fuca Ridge basaltic glasses. *Earth and Planetary Science Letters*, 90(1), 87–104. [https://doi.org/10.1016/0012-821X\(88\)90114-8](https://doi.org/10.1016/0012-821X(88)90114-8)
- Dixon, J. E., Stolper, E. M., & Holloway, J. R. (1995). An Experimental study of water and carbon dioxide solubilities in mid-ocean ridge basaltic liquids. Part I: Calibration and solubility models. *Journal of Petrology*, 36(6), 1607–1631. <https://doi.org/10.1093/oxfordjournals.petrology.a037267>
- Driesner, T., & Heinrich, C. A. (2007). The system H_2O –NaCl. Part I: Correlation formulae for phase relations in temperature–pressure–composition space from 0 to 1000°C, 0 to 5000 bar, and 0 to 1 XNaCl. *Geochimica et Cosmochimica Acta*, 71(20), 4880–4901. <https://doi.org/10.1016/j.gca.2006.01.033>
- Ella, C. Y. (2014). *Volcanology of the Troodos Ophiolite (Cyprus) and mechanisms of accretion of the upper oceanic crust*. Cardiff University. Retrieved from <http://orca.cf.ac.uk/id/eprint/73633>
- Escrig, S., Bézou, A., Langmuir, C. H., Michael, P. J., & Arculus, R. (2012). Characterizing the effect of mantle source, subduction input and melting in the Fonualei Spreading Center, Lau Basin: Constraints on the origin of the boninitic signature of the back-arc lavas. *Geochemistry, Geophysics, Geosystems*, 13(10), Q10008. <https://doi.org/10.1029/2012GC004130>
- Fine, G., & Stolper, E. (1986). Dissolved carbon dioxide in basaltic glasses: Concentrations and speciation. *Earth and Planetary Science Letters*, 76(3), 263–278. [https://doi.org/10.1016/0012-821X\(86\)90078-6](https://doi.org/10.1016/0012-821X(86)90078-6)
- Fleet, A. J., & Robertson, A. H. F. (1980). Ocean-ridge metalliferous and pelagic sediments of the Semail Nappe, Oman. *Journal of the Geological Society*, 137(4), 403–422. <https://doi.org/10.1144/gsjgs.137.4.0403>
- Fonseca, R. O. C., Kirchenbaur, M., Ballhaus, C., Münker, C., Zirner, A., Gerdes, A., et al. (2017). Fingerprinting fluid sources in Troodos ophiolite complex orbicular glasses using high spatial resolution isotope and trace element geochemistry. *Geochimica et Cosmochimica Acta*, 200(23), 145–166. <https://doi.org/10.1016/j.gca.2016.12.012>
- Fonseca, R. O. C., Michely, L. T., Kirchenbaur, M., Prytulak, J., Ryan, J., Hauke, K., et al. (2020). Formation mechanisms of macroscopic globules in andesitic glasses from the Izu–Bonin–Mariana forearc (IODP Expedition 352). *Contributions to Mineralogy and Petrology*, 176(1), 2. <https://doi.org/10.1007/s00410-020-01756-3>
- Friedrich, O., Norris, R. D., & Erbacher, J. (2012). Evolution of middle to late Cretaceous oceans—A 55 m.y. Record of Earth's temperature and carbon cycle. *Geology*, 40(2), 107–110. <https://doi.org/10.1130/G32701.1>
- Fuchs, S., Hannington, M. D., & Petersen, S. (2019). Diving gold in seafloor polymetallic massive sulfide systems. *Mineralium Deposita*, 54(6), 789–820. <https://doi.org/10.1007/s00126-019-00895-3>
- Gass, I. G., MacLeod, C. J., Murton, B. J., Panayiotou, A., Simonian, K. O., & Xenophontos, C. (1994). *The geology of the southern Troodos transform fault zone*. Nicosia. Geological Survey Department Cyprus, Ministry of Agriculture, Natural Resources and Environment.
- Gilgen, S. A., Diamond, L. W., & Mercolli, I. (2016). Sub-seafloor epidiosite alteration: Timing, depth and stratigraphic distribution in the Semail ophiolite, Oman. *Lithos*, 260, 191–210. <https://doi.org/10.1016/j.lithos.2016.05.014>
- Gilgen, S. A., Diamond, L. W., Mercolli, I., Al-Tobi, K., Maudment, D. W., Close, R., & Al-Towaya, A. (2014). Volcanostratigraphic controls on the occurrence of massive Sulfide deposits in the Semail ophiolite, Oman. *Economic Geology*, 109(6), 1585–1610. <https://doi.org/10.2113/econgeo.109.6.1585>
- Gillis, K. M., & Banerjee, N. R. (2000). Hydrothermal alteration patterns in supra-subduction zone ophiolites. *Special Paper - Geological Society of America*, 349, 283–297. <https://doi.org/10.1130/0-8137-2349-3.283>
- Guilmette, C., Smit, M. A., van Hinsbergen, D. J. J., Gürer, D., Corfu, F., Charette, B., et al. (2018). Forced subduction initiation recorded in the sole and crust of the Semail Ophiolite of Oman. *Nature Geoscience*, 11(9), 688–695. <https://doi.org/10.1038/s41561-018-0209-2>
- Hahn, D., Hilton, D. R., Castillo, P. R., Hawkins, J. W., Hanan, B. B., & Hauri, E. H. (2012). An overview of the volatile systematics of the Lau Basin – Resolving the effects of source variation, magmatic degassing and crustal contamination. *Geochimica et Cosmochimica Acta*, 85, 88–113. <https://doi.org/10.1016/j.gca.2012.02.007>
- Hannington, M. D., Galley, A. G., Herzig, P. M., & Petersen, S. (1998). Comparison of the TAG mound and stockwork complex with Cyprus-type, massive sulfide deposits. In *Proceedings of the Ocean Drilling Program, 158 Scientific Results*. <https://doi.org/10.2973/odp.proc.sr.158.217.1998>
- Hara, K., & Kurihara, T. (2017). Radiolarian age and lithostratigraphy of Late Cretaceous pelagic sediments overlying basaltic extrusive rocks, northern Oman mountains. *Ophioliti*, 42(1). <https://doi.org/10.4454/ofioliti.v42i2.446>
- Hay, W. W. (2009). Cretaceous oceans and ocean modeling. *Cretaceous ocean redbeds*. <https://doi.org/10.2110/sepmsp.091.233>
- Hughes, E. C., Buse, B., Kearns, S. L., Blundy, J. D., Kilgour, G., & Mader, H. M. (2019). Low analytical totals in EPMA of hydrous silicate glass due to sub-surface charging: Obtaining accurate volatiles by difference. *Chemical Geology*, 505, 48–56. <https://doi.org/10.1016/j.chemgeo.2018.11.015>
- Humphris, S. E., & Klein, F. (2018). Progress in deciphering the controls on the geochemistry of fluids in seafloor hydrothermal systems. *Annual Review of Marine Science*, 10(1), 315–343. <https://doi.org/10.1146/annurev-marine-121916-063233>

- Hürlimann, N., Müntener, O., Ulmer, P., Nandedkar, R., Chiaradia, M., & Ovtcharova, M. (2016). Primary magmas in continental arcs and their differentiated products: Petrology of a post-plutonic dyke suite in the tertiary Adamello Batholith (Alps). *Journal of Petrology*, 57(3), 495–534. <https://doi.org/10.1093/ptrology/egw016>
- Ishikawa, T., Nagaishi, K., & Umino, S. (2002). Boninitic volcanism in the Oman ophiolite: Implications for thermal condition during transition from spreading ridge to arc. *Geology*, 30(10), 899–902. [https://doi.org/10.1130/0091-7613\(2002\)030<0899:BVITOO>2.0.CO;2](https://doi.org/10.1130/0091-7613(2002)030<0899:BVITOO>2.0.CO;2)
- Jenner, F. E., Hauri, E. H., Bullock, E. S., König, S., Arculus, R. J., Mavrogenes, J. A., et al. (2015). The competing effects of sulfide saturation versus degassing on the behavior of the chalcophile elements during the differentiation of hydrous melts. *Geochemistry, Geophysics, Geosystems*, 16(5), 1490–1507. <https://doi.org/10.1002/2014GC005670>
- Johnson, H. P., Hautala, S. L., Bjorklund, T. A., & Zarnetske, M. R. (2006). Quantifying the North Pacific silica plume. *Geochemistry, Geophysics, Geosystems*, 7(5), Q05011. <https://doi.org/10.1029/2005GC001065>
- Jupp, T. E., & Schultz, A. (2000). A thermodynamic explanation for black smoker temperatures. *Nature*, 403(6772), 880–883. <https://doi.org/10.1038/35002552>
- Jupp, T. E., & Schultz, A. (2004). Physical balances in seafloor hydrothermal convection cells. *Journal of Geophysical Research*, 109(B5), B05101. <https://doi.org/10.1029/2003JB002697>
- Keller, N. S., Arculus, R. J., Hermann, J., & Richards, S. (2008). Submarine back-arc lava with arc signature: Fonualei Spreading Center, northeast Lau Basin, Tonga. *Journal of Geophysical Research*, 113(B8), B08S07. <https://doi.org/10.1029/2007JB005451>
- Korenaga, T., & Korenaga, J. (2008). Subsidence of normal oceanic lithosphere, apparent thermal expansivity, and seafloor flattening. *Earth and Planetary Science Letters*, 268(1), 41–51. <https://doi.org/10.1016/j.epsl.2007.12.022>
- Koschinsky, A., Garbe-Schönberg, D., Sander, S., Schmidt, K., Gennerich, H.-H., & Strauss, H. (2008). Hydrothermal venting at pressure-temperature conditions above the critical point of seawater, 5°S on the Mid-Atlantic Ridge. *Geology*, 36(8), 615–618. <https://doi.org/10.1130/G24726A.1>
- Kusano, Y., Hayashi, M., Adachi, Y., Umino, S., & Miyashita, S. (2014). Evolution of volcanism and magmatism during initial arc stage: Constraints on the tectonic setting of the Oman Ophiolite. *Geological Society, London, Special Publications*, 392(1), 177–193. <https://doi.org/10.1144/SP392.9>
- Kusano, Y., Umino, S., Shinjo, R., Ikei, A., Adachi, Y., Miyashita, S., & Arai, S. (2017). Contribution of slab-derived fluid and sedimentary melt in the incipient arc magmas with development of the paleo-arc in the Oman Ophiolite. *Chemical Geology*, 449, 206–225. <https://doi.org/10.1016/j.chemgeo.2016.12.012>
- Lange, R. A., & Carmichael, I. S. E. (1987). Densities of Na₂O-K₂O-CaO-MgO-FeO-Fe₂O₃-Al₂O₃-TiO₂-SiO₂ liquids: New measurements and derived partial molar properties. *Geochimica et Cosmochimica Acta*, 51(11), 2931–2946. [https://doi.org/10.1016/0016-7037\(87\)90368-1](https://doi.org/10.1016/0016-7037(87)90368-1)
- Le Bas, M. J. (2000). IUGS reclassification of the high-Mg and picritic volcanic rocks. *Journal of Petrology*, 41(10), 1467–1470. <https://doi.org/10.1093/ptrology/41.10.1467>
- Lytle, M. L., Kelley, K. A., Hauri, E. H., Gill, J. B., Papia, D., & Arculus, R. J. (2012). Tracing mantle sources and Samoan influence in the northwestern Lau back-arc basin. *Geochemistry, Geophysics, Geosystems*, 13(10), Q10019. <https://doi.org/10.1029/2012GC004233>
- MacLeod, C. J., Johan Lissenberg, C., & Bibby, L. E. (2013). “Moist MORB” axial magmatism in the Oman ophiolite: The evidence against a mid-ocean ridge origin. *Geology*, 41(4), 459–462. <https://doi.org/10.1130/G33904.1>
- Mandeville, C. W., Webster, J. D., Rutherford, M. J., Taylor, B. E., Timbal, A., & Faure, K. (2002). Determination of molar absorptivities for infrared absorption bands of H₂O in andesitic glasses. *American Mineralogist*, 87(7), 813–821. <https://doi.org/10.2138/am-2002-0702>
- Mantis, M. (1971). Palaeontological evidence defining the age of the Troodos Pillow Lava series in Cyprus. *Cypriakos Logos*, 3, 202–208.
- Martin, A. J., Keith, M., Parvaz, D. B., McDonald, I., Boyce, A. J., McFall, K. A., et al. (2020). Effects of magmatic volatile influx in mafic VMS hydrothermal systems: Evidence from the Troodos ophiolite, Cyprus. *Chemical Geology*, 531, 119325. <https://doi.org/10.1016/j.chemgeo.2019.119325>
- Marty, B., Sano, Y., & France-Lanord, C. (2001). Water-saturated oceanic lavas from the Manus Basin: Volatile behaviour during assimilation–fractional crystallisation–degassing (AFCD). *Journal of Volcanology and Geothermal Research*, 108(1), 1–10. [https://doi.org/10.1016/S0377-0273\(00\)00275-4](https://doi.org/10.1016/S0377-0273(00)00275-4)
- McDermott, J. M., Sylva, S. P., Ono, S., German, C. R., & Seewald, J. S. (2018). Geochemistry of fluids from Earth's deepest ridge-crest hot-springs: Piccard hydrothermal field, Mid-Cayman Rise. *Geochimica et Cosmochimica Acta*, 228, 95–118. <https://doi.org/10.1016/j.gca.2018.01.021>
- Mehegan, J. M. (1988). *Temporal, spatial and chemical evolution of the Troodos ophiolite lavas, Cyprus: Supra-subduction zone volcanism in the Tethys sea*. Halifax. Dalhousie University.
- Miyashita, S., Adachi, Y., & Umino, S. (2003). Along-axis magmatic system in the northern Oman ophiolite: Implications of compositional variation of the sheeted dike complex. *Geochemistry, Geophysics, Geosystems*, 4(9), 8617. <https://doi.org/10.1029/2001GC000235>
- Monecke, T., Petersen, S., & Hannington, M. D. (2014). Constraints on water depth of massive sulfide formation: Evidence from modern seafloor hydrothermal systems in arc-related settings. *Economic Geology*, 109(8), 2079–2101. <https://doi.org/10.2113/econgeo.109.8.2079>
- Moore, G. (2008). Interpreting H₂O and CO₂ contents in melt inclusions: Constraints from solubility experiments and modeling. *Reviews in Mineralogy and Geochemistry*, 69(1), 333–362. <https://doi.org/10.2138/rmg.2008.69.9>
- Morag, N., Golan, T., Katzir, Y., Coble, M. A., Kitajima, K., & Valley, J. W. (2020). The origin of plagiogranites: Coupled SIMS O isotope ratios, U–Pb dating and trace element composition of zircon from the Troodos Ophiolite, Cyprus. *Journal of Petrology*, 61(5), egaa057. <https://doi.org/10.1093/ptrology/egaa057>
- Morgan, G. B., & London, D. (2005). Effect of current density on the electron microprobe analysis of alkali aluminosilicate glasses. *American Mineralogist*, 70(9), 1131–1138. <https://doi.org/10.2138/am.2005.1769>
- Mortlock, R. A., Froelich, P. N., Feely, R. A., Massoth, G. J., Butterfield, D. A., & Lupton, J. E. (1993). Silica and germanium in Pacific Ocean hydrothermal vents and plumes. *Earth and Planetary Science Letters*, 119(3), 365–378. [https://doi.org/10.1016/0012-821X\(93\)90144-X](https://doi.org/10.1016/0012-821X(93)90144-X)
- Moss, R., Scott, S. D., & Binns, R. A. (2001). Gold content of eastern Manus basin volcanic rocks: Implications for enrichment in associated hydrothermal precipitates. *Economic Geology*, 96(1), 91–107. <https://doi.org/10.2113/gsecongeo.96.1.91>
- Nehlig, P., Juteau, T., Bendel, V., & Cotten, J. (1994). The root zones of oceanic hydrothermal systems: Constraints from the Samail Ophiolite (Oman). *Journal of Geophysical Research*, 99(B3), 4703–4713. <https://doi.org/10.1029/93JB02663>
- Newman, S., & Lowenstern, J. B. (2002). VOLATILECALC: A silicate melt-H₂O-CO₂ solution model written in Visual Basic for excel. *Computers and Geosciences*. [https://doi.org/10.1016/S0098-3004\(01\)00081-4](https://doi.org/10.1016/S0098-3004(01)00081-4)
- Newman, S., Stolper, E. M., & Stern, R. (2000). H₂O and CO₂ in magmas from the Mariana arc and back arc systems. *Geochemistry, Geophysics, Geosystems*, 1(5), 1013. <https://doi.org/10.1029/1999GC000027>
- Ochs, F. A., & Lange, R. A. (1999). The density of hydrous magmatic liquids. *Science*, 283(406), 1314–1317. <https://doi.org/10.1126/science.283.5406.1314>

- Osozawa, S., Shinjo, R., Lo, C.-H., Jahn, B.-M., Hoang, N., Sasaki, M., et al. (2012). Geochemistry and geochronology of the Troodos ophiolite: An SSZ ophiolite generated by subduction initiation and an extended episode of ridge subduction? *Lithosphere*, 4(6), 497–510. <https://doi.org/10.1130/L205.1>
- Pälike, H., Lyle, M. W., Nishi, H., Raffi, I., Ridgwell, A., Gamage, K., et al. (2012). A Cenozoic record of the equatorial Pacific carbonate compensation depth. *Nature*, 488(7413), 609–614. <https://doi.org/10.1038/nature11360>
- Pan, A., Yang, Q., Zhou, H., Ji, F., Wang, H., & Pancost, R. D. (2018). Geochemical impacts of hydrothermal activity on surface deposits at the Southwest Indian Ridge. *Deep Sea Research Part I: Oceanographic Research Papers*, 139, 1–13. <https://doi.org/10.1016/j.dsr.2018.05.009>
- Patriat, M., Falloon, T., Danyushevsky, L., Collot, J., Jean, M. M., Hoernle, K., et al. (2019). Subduction initiation terranes exposed at the front of a 2 Ma volcanically-active subduction zone. *Earth and Planetary Science Letters*, 508, 30–40. <https://doi.org/10.1016/j.epsl.2018.12.011>
- Patten, C. G. C., Pitcairn, I. K., Alt, J. C., Zack, T., Lahaye, Y., Teagle, D. A. H., & Markdahl, K. (2019). Metal fluxes during magmatic degassing in the oceanic crust: Sulfide mineralisation at ODP site 786B, Izu-Bonin forearc. *Mineralium Deposita*, 55, 469–489. <https://doi.org/10.1007/s00126-019-00900-9>
- Pearce, J. A., Alabaster, T., Shelton, A. W., & Searle, M. P. (1981). The Oman ophiolite as a Cretaceous arc-basin complex: Evidence and Implications. *Philosophical Transactions of the Royal Society of London - Series A: Mathematical and Physical Sciences*, 300(1454), 299–317. <https://doi.org/10.1098/rsta.1981.0066>
- Pearce, J. A., Lippard, S. J., & Roberts, S. (1984). Characteristics and tectonic significance of supra-subduction zone ophiolites. *Geological Society, London, Special Publications*, 16(1), 77–94. <https://doi.org/10.1144/GSL.SP.1984.016.01.06>
- Pearce, J. A., & Reagan, M. K. (2019). Identification, classification, and interpretation of boninites from Anthropocene to Eoarchean using Si-Mg-Ti systematics. *Geosphere*, 15(4), 1008–1037. <https://doi.org/10.1130/GES01661.1>
- Pearce, J. A., & Robinson, P. T. (2010). The Troodos ophiolitic complex probably formed in a subduction initiation, slab edge setting. *Gondwana Research*, 18(1), 60–81. <https://doi.org/10.1016/j.gr.2009.12.003>
- Portnyagin, M. V., Danyushevsky, L. V., & Kamenetsky, V. S. (1997). Coexistence of two distinct mantle sources during formation of ophiolites: A case study of primitive pillow-lavas from the lowest part of the volcanic section of the Troodos Ophiolite, Cyprus. *Contributions to Mineralogy and Petrology*, 128(2), 287–301. <https://doi.org/10.1007/s004100050309>
- Putirka, K. D. (2008). Thermometers and barometers for volcanic systems. *Reviews in Mineralogy and Geochemistry*, 69(1), 61–120. <https://doi.org/10.2138/rmg.2008.69.3>
- Quandt, D., Micheuz, P., Kurz, W., & Krenn, K. (2018). Microtextures and fluid inclusions from vein minerals hosted in the Pillow Lavas of the Troodos supra-subduction zone. *Lithosphere*, 10(4), 566–578. <https://doi.org/10.1130/L696.1>
- Regelous, M., Haase, K. M., Freund, S., Keith, M., Weinzierl, C. G., Beier, C., et al. (2014). Formation of the Troodos Ophiolite at a triple junction: Evidence from trace elements in volcanic glass. *Chemical Geology*, 386, 66–79. <https://doi.org/10.1016/j.chemgeo.2014.08.006>
- Ribeiro, J. M., Stern, R. J., Kelley, K. A., Shaw, A. M., Martinez, F., & Ohara, Y. (2015). Composition of the slab-derived fluids released beneath the Mariana forearc: Evidence for shallow dehydration of the subducting plate. *Earth and Planetary Science Letters*, 418, 136–148. <https://doi.org/10.1016/j.epsl.2015.02.018>
- Rioux, M., Bowring, S., Kelemen, P., Gordon, S., Miller, R., & Dudás, F. (2013). Tectonic development of the Samail ophiolite: High-precision U-Pb zircon geochronology and Sm-Nd isotopic constraints on crustal growth and emplacement. *Journal of Geophysical Research: Solid Earth*, 118(5), 2085–2101. <https://doi.org/10.1002/jgrb.50139>
- Rioux, M., Garber, J., Bauer, A., Bowring, S., Searle, M., Kelemen, P., & Hacker, B. (2016). Synchronous formation of the metamorphic sole and igneous crust of the Semail ophiolite: New constraints on the tectonic evolution during ophiolite formation from high-precision U–Pb zircon geochronology. *Earth and Planetary Science Letters*, 451, 185–195. <https://doi.org/10.1016/j.epsl.2016.06.051>
- Rioux, M., Garber, J. M., Searle, M., Kelemen, P., Miyashita, S., Adachi, Y., & Bowring, S. (2021). High-precision U-Pb zircon dating of late magmatism in the Semail ophiolite: A record of subduction initiation. *Journal of Geophysical Research: Solid Earth*, e2020JB020758. <https://doi.org/10.1029/2020JB020758>
- Roberge, J., Wallace, P. J., White, R. V., & Coffin, M. F. (2005). Anomalous uplift and subsidence of the Ontong Java Plateau inferred from CO₂ contents of submarine basaltic glasses. *Geology*, 33(6), 501–504. <https://doi.org/10.1130/G21142.1>
- Robertson, A. (2004). Development of concepts concerning the genesis and emplacement of Tethyan ophiolites in the Eastern Mediterranean and Oman regions. *Earth-Science Reviews*, 66(3), 331–387. <https://doi.org/10.1016/j.earscirev.2004.01.005>
- Robertson, A. H. F. (1975). Cyprus umbers: Basalt-sediment relationships on a Mesozoic ocean ridge. *Journal of the Geological Society*, 131(5), 511–531. <https://doi.org/10.1144/gsjgs.131.5.0511>
- Robertson, A. H. F., Clift, P. D., Degnan, P. J., & Jones, G. (1991). Palaeogeographic and palaeotectonic evolution of the Eastern Mediterranean Neotethys. *Palaeogeography, Palaeoclimatology, Palaeoecology*, 87(1), 289–343. [https://doi.org/10.1016/0031-0182\(91\)90140-M](https://doi.org/10.1016/0031-0182(91)90140-M)
- Robertson, A. H. F., & Fleet, A. J. (1986). Geochemistry and palaeo-oceanography of metalliferous and pelagic sediments from the Late Cretaceous Oman ophiolite. *Marine and Petroleum Geology*, 3(4), 315–317. [https://doi.org/10.1016/0264-8172\(86\)90036-X](https://doi.org/10.1016/0264-8172(86)90036-X)
- Robertson, A. H. F., & Hudson, J. D. (1974). Pelagic sediments in the Cretaceous and Tertiary history of the Troodos Massif, Cyprus. In K. J. Hsü, & H. C. Jenkyns (Eds.), *Pelagic sediments: On land and under the sea* (pp. 403–436). Oxford: Blackwell Scientific Publications Ltd. <https://doi.org/10.1002/9781444304855.ch19>
- Robinson, P. T., Melson, W. G., O'Hearn, T., & Schmincke, H.-U. (1983). Volcanic glass compositions of the Troodos ophiolite, Cyprus. *Geology*, 11(7), 400–404. [https://doi.org/10.1130/0091-7613\(1983\)11<400:VGCOTT>2.0.CO;2](https://doi.org/10.1130/0091-7613(1983)11<400:VGCOTT>2.0.CO;2)
- Roedder, E. (1984). Fluid inclusions. *Reviews in Mineralogy* (Vol. 12). Mineralogical Society of America.
- Slater, J. G., Abbott, D., & Thiede, J. (1977). Paleobathymetry and Sediments of the Indian Ocean. *Indian Ocean Geology and Biostratigraphy*. <https://doi.org/10.1029/SP009p0025>
- Seyfried, W. E., Jr., Ding, K., Berndt, M. E., & Chen, X. (1997). Experimental and theoretical controls on the composition of mid-ocean ridge hydrothermal fluids. In C. Tucker Barrie, & M. D. Hannington (Eds.), *Volcanic associated massive sulfide deposits: Processes and examples in modern and ancient settings* (Vol. 8, pp. 181–200). Society of Economic Geologists. <https://doi.org/10.5382/Rev.08.08>
- Shimizu, K., Shimizu, N., Sano, T., Matsubara, N., & Sager, W. (2013). Paleo-elevation and subsidence of ~145 Ma Shatsky Rise inferred from CO₂ and H₂O in fresh volcanic glass. *Earth and Planetary Science Letters*, 383, 37–44. <https://doi.org/10.1016/j.epsl.2013.09.023>
- Shishkina, T. A., Botcharnikov, R. E., Holtz, F., Almeev, R. R., & Portnyagin, M. V. (2010). Solubility of H₂O- and CO₂-bearing fluids in tholeiitic basalts at pressures up to 500 MPa. *Chemical Geology*, 277(1), 115–125. <https://doi.org/10.1016/j.chemgeo.2010.07.014>
- Small, C. (1994). A global analysis of mid-ocean ridge axial topography. *Geophysical Journal International*, 116(1), 64–84. <https://doi.org/10.1111/j.1365-246X.1994.tb02128.x>

- Spooner, E. T. C. (1980). Cu-Pyrite Mineralization and seawater convection in oceanic crust – The ophiolitic ore deposits of Cyprus. In D. W. Strangway (Ed.), *The continental crust and its mineral deposits* (Vol. 20, pp. 685–704). Geological Association of Canada Special Paper.
- Spooner, E. T. C., & Bray, C. J. (1985). Fluid-inclusion evidence for boiling at 370°C in the stockwork of the Lasail ophiolitic hydrothermal massive-sulfide deposit, Oman (abstract). *Eos Transactions AGU*, 66, 724–725.
- Ulmer, P., Kaegi, R., & Müntener, O. (2018). Experimentally derived intermediate to silica-rich arc magmas by fractional and equilibrium crystallization at 1-0 GPa: An evaluation of phase relationships, compositions, liquid lines of descent and oxygen fugacity. *Journal of Petrology*, 59(1), 11–58. <https://doi.org/10.1093/petrology/egy017>
- Umino, S. (2012). Emplacement mechanism of off-axis large submarine lava field from the Oman Ophiolite. *Journal of Geophysical Research*, 117, B11210. <https://doi.org/10.1029/2012JB009198>
- Umino, S., Yanai, S., Jaman, A. R., Nakamura, Y., & Iiyama, J. T. (1990). The transition from spreading to subduction: Evidence from the Se-mail Ophiolite, northern Oman Mountains. In *Oceanic Crustal Analogues: Proceedings of the Symposium "Troodos 1987"* (pp. 375–384). Nicosia. Cyprus Geological Survey Department.
- Urquhart, E., & Banner, F. T. (1994). Biostratigraphy of the supra-ophiolite sediments of the Troodos Massif, Cyprus: The Cretaceous Perapedhi, Kannaviou, Moni and Kathikas formations. *Geological Magazine*, 131(4), 499–518. <https://doi.org/10.1017/S0016756800012127>
- Van Andel, T. H. (1975). Mesozoic/cenozoic calcite compensation depth and the global distribution of calcareous sediments. *Earth and Planetary Science Letters*, 26(2), 187–194. [https://doi.org/10.1016/0012-821X\(75\)90086-2](https://doi.org/10.1016/0012-821X(75)90086-2)
- von Aulock, F. W., Kennedy, B. M., Schipper, C. L., Castro, J. M., Martin, D. E., Oze, C., et al. (2014). Advances in Fourier transform infrared spectroscopy of natural glasses: From sample preparation to data analysis. *Lithos*, 52–64. <https://doi.org/10.1016/j.lithos.2014.07.017>
- Von Damm, K. L., Lilley, M. D., Shanks, W. C., Brockington, M., Bray, A. M., O'Grady, K. M., et al. (2003). Extraordinary phase separation and segregation in vent fluids from the southern East Pacific Rise. *Earth and Planetary Science Letters*, 206(3), 365–378. [https://doi.org/10.1016/S0012-821X\(02\)01081-6](https://doi.org/10.1016/S0012-821X(02)01081-6)
- Von Damm, K. L., Oosting, S. E., Kozlowski, R., Buttermore, L. G., Colodner, D. C., Edmonds, H. N., et al. (1995). Evolution of East Pacific Rise hydrothermal vent fluids following a volcanic eruption. *Nature*, 375, 47–50. <https://doi.org/10.1038/375047a0>
- Webber, A. P., Roberts, S., Murton, B. J., & Hodgkinson, M. R. S. (2015). Geology, sulfide geochemistry and supercritical venting at the Beebe Hydrothermal Vent Field, Cayman Trough. *Geochemistry, Geophysics, Geosystems*, 16(8), 2661–2678. <https://doi.org/10.1002/2015GC005879>
- Wickham, H. (2016). *ggplot2: Elegant graphics for data analysis*. New York: Springer-Verlag.
- Witham, F., Blundy, J., Kohn, S. C., Lesne, P., Dixon, J., Churakov, S. V., & Botcharnikov, R. (2012). SolEx: A model for mixed COHSL-volatile solubilities and exsolved gas compositions in basalt. *Computers & Geosciences*, 45, 87–97. <https://doi.org/10.1016/j.cageo.2011.09.021>
- Woelki, D., Michael, P., Regelous, M., & Haase, K. (2020). Enrichment of H₂O and fluid-soluble trace elements in the Troodos Ophiolite: Evidence for a near-trench origin. *Lithos*, 356–357, 105299. <https://doi.org/10.1016/j.lithos.2019.105299>
- Woelki, D., Regelous, M., Haase, K. M., Romer, R. H. W., & Beier, C. (2018). Petrogenesis of boninitic lavas from the Troodos Ophiolite, and comparison with Izu–Bonin–Mariana fore-arc crust. *Earth and Planetary Science Letters*, 498, 203–214. <https://doi.org/10.1016/j.epsl.2018.06.041>
- Wysoczanski, R. J., Wright, I. C., Gamble, J. A., Hauri, E. H., Luhr, J. F., Eggins, S. M., & Handler, M. R. (2006). Volatile contents of Kermadec Arc–Havre Trough pillow glasses: Fingerprinting slab-derived aqueous fluids in the mantle sources of arc and back-arc lavas. *Journal of Volcanology and Geothermal Research*, 152(1), 51–73. <https://doi.org/10.1016/j.jvolgeores.2005.04.021>